# Phase Equilibria of the Lyngdal Granodiorite (Norway): Implications for the Origin of Metaluminous Ferroan Granitoids.

Michel Bogaerts, Bruno Scaillet, Jacqueline Vander Auwera

## To cite this version:

Michel Bogaerts, Bruno Scaillet, Jacqueline Vander Auwera. Phase Equilibria of the Lyngdal Granodiorite (Norway): Implications for the Origin of Metaluminous Ferroan Granitoids.. Journal of Petrology, 2006, 47, pp.2405-2431. 10.1093/petrology/egl049 . hal-00101447

HAL Id: hal-00101447
https://insu.hal.science/hal-00101447

Submitted on 7 May 2009

# Phase Equilibria of the Lyngdal Granodiorite (Norway): Implications for the Origin of Metaluminous Ferroan Granitoids

MICHEL BOGAERTS[1,*], BRUNO SCAILLET[2] and JACQUELINE VANDER AUWERA[1]

[1] U.R. PÉTROLOGIE ET GÉOCHIMIE ENDOGÈNE (B20), DÉPARTEMENT DE GÉOLOGIE,
UNIVERSITÉ DE LIÈGE B-4000 SART TILMAN, BELGIUM
[2] ISTO-CNRS UMR 6113, 1A RUE DE LA FÉROLLERIE, ORLÉANS, 45071 CEDEX 2, FRANCE

## ABSTRACT

The Proterozoic (950 Ma) Lyngdal granodiorite of southern Norway belongs to a series of hornblende–biotite metaluminous ferroan granitoids (HBG suite) coeval with the post-collisional Rogaland Anorthosite–Mangerite–Charnockite (AMC) suite. This granitoid massif shares many geochemical characteristics with rapakivi granitoids, yet granodiorites dominate over granites. To constrain both crystallization (P, T, $fO_2$, $H_2O$ in melt) and magma generation conditions, we performed crystallization experiments on two samples of the Lyngdal granodiorite (with 60 and 65 wt % $SiO_2$) at 4–2 kbar, mainly at $fO_2$ of NNO (nickel–nickel oxide) to NNO + 1, and under fluid-saturated conditions with various $H_2O$–$CO_2$ ratios for each temperature. Comparison between experimental phase equilibria and the mineral assemblage in the Lyngdal granodiorite indicates that it crystallized between 4 and 2 kbar, from a magma with 5–6 wt % $H_2O$ at an $fO_2$ of NNO to NNO + 1. These oxidized and wet conditions sharply contrast with the dry and reduced conditions inferred for the petrogenesis of the AMC suite and many other rapakivi granites worldwide. The high liquidus temperature and $H_2O$ content of the Lyngdal granodiorite imply that it is not a primary magma produced by the partial melting of the crust but is derived by the fractionation of a mafic magma. Lyngdal-type magmas appear to have volcanic equivalents in the geological record. In particular, our results show that oxidized high-silica rhyolites, such as the Bishop Tuff, could be derived via fractionation of oxidized intermediate magmas and do not necessarily represent primary crustal melts. This study underlines the great variability of crystallization conditions (from anhydrous to hydrous and reduced to oxidized) and petrogenetic processes among the metaluminous ferroan magmas of intermediate compositions (granodiorites, quartz mangerites, quartz latites), suggesting that there is not a single model to explain these rocks.

KEY WORDS: *ferroan granitoids; crystallization conditions; experiments; Norway; Sveconorwegian; Bishop Tuff*

## INTRODUCTION

Metaluminous ferroan granitoids [using the terminology of Frost *et al*. (2001)] have been reported from many different areas and geological epochs, but are particularly common in mid-Proterozoic terranes. In particular, the magmatic association characterized by massif anorthosites and granitoids is restricted to the Proterozoic and is commonly referred to as an AMCG complex (acronym of Anorthosite–Mangerite–Charnockite–Granite). This study focuses on such a petrogenetic association. The majority of granitoids associated with massif anorthosites can be classified into two main types: (1) hypersthene-dominant granitoids, i.e. quartz mangerites (Opx monzonites)–charnockites (Opx granites); (2) hornblende–biotite granitoids. Some of these latter plutons locally display rapakivi textures and then are called rapakivi granites. Transitional facies, with orthopyroxene rimmed by hornblende, exist in a number of complexes (e.g.Emslie *et al*., 1994). Both types of plutons are metaluminous ferroan granitoids but show a large variation in their MALI index [$(Na_2O + K_2O) – CaO$ in wt %], from calc-alkalic to alkalic as indicated in Fig. 1. All the granitoids and volcanic rocks discussed in this paper (Fig. 1) are metaluminous with ASI $\leq 1$ [molar ratio of $Al_2O_3/(CaO – 3{\cdot}3P_2O_5 + Na_2O + K_2O)$] and agpaitic index AI < 1 [molar ratio $(K_2O + Na_2O)/Al_2O_3$]. Ferroan peralkaline intrusions (e.g. the sodic series of the Pikes Peak batholith: Smith *et al.*, 1999) are not considered here.

In many AMCG complexes, ilmenite is the dominant or sole Fe–Ti oxide and mineral equilibria studies suggest that both types of pluton crystallized from low $fO_2$ and $H_2O$-poor magmas (e.g. Frost & Frost, 1997). Two main models have been proposed to explain the link between anorthosite massifs and associated granitic plutons in the AMCG complexes from North America (e.g. Laramie anorthositic complex, Nain Province). Emslie *et al.* (1994) proposed that the anorthosites ultimately formed from a mantle-derived magma differentiating in the lower crust, whereas the granitic magmas were produced by melting of the lower crust. In their model, there is no parent–daughter relationship between anorthosite and granite magmas and a wide range of felsic magmas associated with the anorthosite massifs is expected. The second model relies, in part, on the observation that granitoids from AMCG complexes usually have similar bulk-rock compositions and crystallization conditions (Frost & Frost, 1997; Frost *et al*., 2002; Anderson *et al*., 2003). According to this model the reduced and $H_2O$-poor metaluminous ferroan granitoids are ultimately derived from tholeiitic magmas, from which the massif anorthosites are proposed to crystallize (the so-called ‘tholeiite connection’); the acid magmas are considered to be either differentiation products of parental basalts, or, and more likely, partial melts resulting from the anatexis of the differentiated products of such underplated basalts.

In both models, the implicit assumption is that the elevated iron content of the melt is due to the low $fO_2$ prevailing in the source, which prevents Fe–Ti oxide crystallization during the early stages of differentiation as in arc magmas series (Martel *et al*., 1999). However, there exist a number of metaluminous ferroan granitoids that, despite having elevated iron contents, display a significantly higher redox state than those ferroan granitoids of clear tholeiitic affinity (e.g. Dall'Agnol *et al*., 1999). In the tholeiite model, one way to produce the oxidized granitoids contemporaneous with the reduced ones is through contamination of the parental magma by oxidized crust (e.g. Frost & Frost, 1997; Anderson *et al*., 2003). However, Anderson & Morrison (2005) have observed variations of $fO_2$ among the ferroan granitoids at the scale of a continent, which they related to the diversity in $fO_2$ of their source in the lower crust. Such a large-scale trend suggests that oxidized, metaluminous ferroan granitoids may be disconnected from reduced granitoids.

We base our work on the well-known geological setting of SW Norway, in which both types of metaluminous ferroan granitoids (opx- and hornblende–biotite granitoids) and anorthosite massifs have been documented within the Precambrian basement (e.g. Duchesne *et al*., 1985✚; Duchesne & Wilmart, 1997✚; Vander Auwera *et al*., 2003✚). These magmatic rocks were emplaced during the post-collisional stage of the orogeny between ∼960 and 920 Ma. Previous experimental studies relevant to this area (Vander Auwera & Longhi, 1994✚; Vander Auwera *et al*., 1998✚; Longhi *et al*., 1999✚) have only considered the origin of the opx-bearing rocks, i.e. the anorthosites and their potential derivatives such as charnockites (hereafter referred to as the AMC suite for Anorthosite–Mangerite–Charnockite). These studies have shown conclusively that in southern Norway the petrogenesis of the AMC suite can be modelled by fractional crystallization of a dry jotunitic (opx-monzodiorite) parent magma evolving under low $fO_2$ conditions.

As noted above, the hornblende–biotite granitoids, although compositionally similar to charnockites, exhibit significant differences in mineralogy, most notably in the abundance of amphibole and magnetite (Bogaerts *et al*., 2003*a*; Vander Auwera *et al*., 2003). The main goal of our experimental work is to constrain the crystallization conditions ($P$, $T$, $fO_2$, $H_2O$ in melt) of these hornblende–biotite granitoids. Such constraints are important to evaluate petrogenetic models for these granitoids in southern Norway.

We have performed phase equilibrium experiments on two representative samples from the Lyngdal granodiorite, a metaluminous ferroan hornblende–biotite granitoid associated with the Rogaland–Vest Agder anorthosite massif in southwestern Norway. Our results, combined with previous studies on the AMC suite (Vander Auwera & Longhi, 1994; Duchesne & Wilmart, 1997; Vander Auwera *et al*., 1998; Bolle *et al*., 2003), suggest that the metaluminous ferroan granitoids of southwestern Norway may be derived from a variety of sources with contrasted redox states and $H_2O$ contents.

Besides their regional implications, our experimental data show that some present-day oxidized high-silica rhyolites can be produced via crystal fractionation of intermediate metaluminous ferroan magmas. The data also provide a framework for a comparison with the voluminous quartz latite ash flows associated with flood basalt events such as those of the Etendeka–Paraná Province, which exhibit a number of similarities to the intermediate ferroan magmas of the AMCG complexes (Table 1, Fig. 1). Our results confirm the complexity of petrogenetic processes at work in producing ferroan magmas.

# GEOLOGICAL BACKGROUND

The Sveconorwegian orogen (1200–900 Ma), which forms the southwestern part of the Baltic Shield, is made up of several Paleo-Mesoproterozoic lithotectonic domains separated by major lineaments (Bingen *et al*., 2001). From east to west (inset of Fig. 2), these domains are the parautochthonous segment (the Eastern Segment) and two allochthonous terranes: the Idefjorden and Telemarkia terranes; the Bamble–Kongsberg (B–K) sector is interpreted as an early Sveconorwegian collision zone between these two terranes (Bingen *et al*., 2005). Assemblage and stacking of these terranes occurred during the main phase of the Sveconorwegian orogeny accompanied by high-grade regional metamorphism (amphibolite to granulite facies) between 1030 and 970 Ma (Bingen & van Breemen, 1998; Bingen & Stein, 2003) in the SW of the Telemarkia terrane (the Rogaland–Vest Agder sector; Bingen *et al*., 2005) and between 980 and 970 Ma in the Eastern Segment (Möller, 1998; Johansson *et al*., 2001). This regional metamorphism was followed by extensive post-collisional magmatism represented by numerous plutons, which preserve their original magmatic paragenesis (no metamorphic overprint or alteration) and can be divided on a petrographic basis into two groups: (1) hornblende–biotite granitoids (Vander Auwera *et al*., 2003); (2) plutons belonging to the charnockitic series (e.g. Duchesne & Wilmart, 1997). The former group is present in all the allochthonous terranes, whereas the latter group is restricted to the southwestern outcropping part of the Telemarkia terrane forming the Rogaland anorthosite province (Duchesne *et al*., 1985). In this study, we restrict our discussion to the Sveconorwegian post-collisional magmatism of the Rogaland anorthositic province and to the hornblende–biotite plutons cropping out in the Telemarkia terrane (Lyngdal, Tranevåg, Holum, Svöfjell, Valle, Rustfjellet, Verhuskjerringi; Fig. 2). Magmatic rocks from the Rogaland anorthositic province (Fig. 1) form the AMC suite (Anorthosite–Mangerite–Charnockite), whereas the associated hornblende–biotite granitoids are termed the HBG suite (Hornblende–Biotite Granitoids), following Vander Auwera *et al.* (2003). The large hornblende–biotite intrusions of the HBG suite define a differentiation trend from 56 to 77 wt % $SiO_2$ (Vander Auwera *et al.*, 2003✚). Small (<5 $km^2$), less differentiated intrusions (Handeland–Tveit and Åseral quartz diorites–monzodiorites: $SiO_2$ between 50 and 61 wt %) were also included by Vander Auwera *et al.* (2003) in the HBG suite (Fig. 1).

The anorthosite complex suite was emplaced at *c*. 930 Ma (Schärer *et al.*, 1996) whereas the Lyngdal granodiorite was emplaced at 950 ± 5 Ma (Pasteels *et al.*, 1979). Zircon dating suggests that the entire HBG suite was emplaced between 960 and 920 Ma (Andersen *et al.*, 2002; Bingen *et al.*, 2006). The Farsund granitoid, dated at 936 Ma, crops out between the AMC suite and the Lyngdal massif, and shows mingling relations between the AMC and HBG suites (Dupont & Vander Auwera, 2002; Dupont *et al.*, 2005, and unpublished data); thus the AMC and HBG suites can be considered coeval.

## The Lyngdal granodiorite

The Lyngdal massif is a large (300 $km^2$) granodioritic intrusion ($SiO_2$ 60–65 wt %: Bogaerts *et al.*, 2003*a*) and is the nearest HBG intrusion to the exposures of the AMC suite (Fig. 2). Its main minerals are plagioclase, K-feldspar, quartz, amphibole, biotite and clinopyroxene (found as inclusions in amphibole and plagioclase). Accessory minerals are Fe–Ti oxides, apatite, zircon, titanite and allanite. The rocks are usually porphyritic, with plagioclase and K-feldspar phenocrysts (average length 1 cm, with a maximum of 2 cm in a few samples) included in a coarse-grained groundmass (average mineral size 2–3 mm; Fig. 3a), consisting of all other minerals, as well as plagioclase and K-feldspar. Plagioclase phenocrysts (anhedral to subhedral) have the same composition as plagioclase in the groundmass and contain inclusions of Fe–Ti oxides and rare clinopyroxenes. They are weakly zoned from $An_{35}$ (andesine core) to $An_{22}$ (oligoclase rim). Myrmekite is commonly developed along the boundaries between plagioclase and K-feldspar. The K-feldspar (in the groundmass or as a phenocryst) is perthitic orthoclase or microcline. K-feldspar phenocrysts (Fig. 3c and d) can contain all other mineral phases as inclusions, suggesting their late crystallization. This is a common feature in granitoids, as discussed by Vernon (1986); the large size of the K-feldspars is probably due to their difficulty to nucleate.

Quartz forms large amoeboid grains around the other minerals. Amphibole is the dominant mafic mineral in Lyngdal but its modal proportion relative to biotite decreases with increasing bulk-rock $SiO_2$ content. Amphibole appears as anhedral poikilitic grains, containing Fe–Ti oxides and accessory minerals (apatite, zircon, allanite, titanite) or as sub-to euhedral grains (Fig. 3a), sometimes included in plagioclase, and in some samples amphibole contains a core of clinopyroxene (Fig. 3b). All amphiboles have $(Ca + Na)_{M4} > 1{\cdot}34$ and $(Na)_{M4} < 0{\cdot}67$ and are thus calcic amphiboles (Leake, 1978; Leake *et al.*, 1997). Their composition is relatively homogeneous in a given sample but exhibits some small variations between samples (edenitic hornblendes and magnesio-hastingites). The cationic ratio $X_{Fe}$ [Fe/(Fe + Mg)] of the amphiboles varies between 0·47 and 0·58 and slightly increases with the $SiO_2$ content of the whole-rock. The $Al_2O_3$ content varies between 9·6 and 11·1 wt %. Biotite is anhedral to euhedral and scarce in the less differentiated samples (~60 wt % $SiO_2$) but becomes more abundant with increasing $SiO_2$ content. Its $X_{Fe}$ varies between 0·47 and 0·51. These $X_{Fe}$ values are similar to those in biotite in other oxidized Proterozoic ferroan granitoids (e.g. Jamon granite, Dall'Agnol *et al.*, 1999). Apatite is abundant and forms large euhedral crystals (up to 5 mm); it is generally included in all other minerals. Zircon is also abundant, forming large euhedral crystals (up to 8 mm), and occurs as inclusions in all the main minerals. Titanite forms anhedral to subhedral grains and is commonly found as coronas around Fe–Ti oxides. Allanite is generally a metamict phase in biotite.

The petrographic observations suggest the following sequence of crystallization: apatite, ilmenite, magnetite and clinopyroxene are probably the liquidus minerals and are followed by amphibole and plagioclase, which are interpreted as crystallizing nearly together with zircon. Biotite appears later and is followed by quartz, potassic feldspar and titanite. Pressures calculated using the Al-in-hornblende geobarometer (Johnson & Rutherford, 1989*a*) are between 3·6 and 5·1 kbar.

## EXPERIMENTAL AND ANALYTICAL PROCEDURES

Two samples from the Lyngdal granodiorite (Table 1) were selected for the experimental study, 98N50 (~60 wt % $SiO_2$) and 98N06 (~65 wt % $SiO_2$), which are the least and most differentiated facies of the pluton, respectively (Bogaerts *et al*., 2003*a*). Several lines of evidence suggest that these samples can be considered as representative of the original magmas. First, their rare earth element (REE) patterns display slight negative Eu anomalies, an observation that is not in favour of plagioclase accumulation. Accumulation of early crystallized apatite/zircon would have enriched the magma in $P_2O_5$/Zr and produced unrealistic high apatite–zircon saturation temperatures. These saturation temperatures are in the range of 1000–800°C, close to the liquidus temperatures of ferroan granites (e.g. Dall'Agnol *et al*., 1999), precluding significant apatite and zircon accumulation (Bogaerts *et al*., 2003*a*; Vander Auwera *et al*., 2003). Second, despite its porphyritic character, the Lyngdal massif does not show structural evidence of crystal accumulation and layering, as observed in some other plutons (e.g. Barbey *et al*., 2001). On the contrary, fine-grained samples collected near the margins of the pluton have compositions similar to the more porphyritic ones (sample MB99N32, Table 1). Sample 98N06 is similar in composition to silicic volcanic rocks (e.g. quartz latites from the Etendeka–Paraná Province: Table 1 and discussion below), which are considered to represent liquid compositions (Ewart *et al*., 1998). This observation does not definitively prove that sample 98N06 is representative of the Lyngdal parent magma but at least shows that it is a plausible composition for a silicate liquid.

The starting products for the crystallization experiments were glasses obtained after two fusions (each at 1400°C and 1 atm for 4 h) of the powdered rock samples. Cleaned Au capsules were successively loaded with weighed amounts of deionized $H_2O$, silver oxalate ($Ag_2C_2O_4$) as a source of $CO_2$, and glass powder. Au capsules were chosen to prevent Fe loss to the container (e.g. Sisson & Grove, 1993). Upon heating, the silver oxalate decomposes to blebs of silver and $CO_2$ and a C–O–H fluid is formed, in which almost all the C forms the $CO_2$ species under the investigated $fO_2$ (see Scaillet *et al*., 1995). For each investigated temperature and each bulk composition, 4–6 capsules were prepared, each with a different initial fluid composition; i.e. the molar $H_2O/(H_2O + CO_2)$ ratio in the fluid, $XH_2O^{in}$, was varied between one [considering the $H_2O$-saturated melt at $P$–$T$ as the standard state: $a_{H2O}$ (melt) = $a_{H2O}$ (fluid) = 1] and 0·5. Fluid-saturated conditions at 4 kbar were achieved by keeping a mass ratio of 15% fluid for 85% silicate powder. In two runs (4 kbar and 1000°C; 2 kbar and 850°C), $H_2O$ was the sole added volatile with the mass ratio $H_2O$/silicate calculated to yield $H_2O$-undersaturated or $H_2O$-saturated melts. The capsules were then welded shut and checked for leaks in an oil-bath at 120°C.

Experiments were mainly performed in an internally heated pressure vessel (IHPV ‘Gros Bleu’) pressurized with $Ar–H_2$ mixtures. The vessel was fitted with an $H_2$-membrane (Scaillet *et al*., 1992) for temperatures below 950°C. One experiment at 2 kbar and 850°C was performed in another IHPV, named 'Basset' (Tables 2 and 3). This vessel can be pressurized only by Ar and imposes oxidized conditions (see below). Temperature in the reaction zone was read by two sheathed type-K thermocouples to check for thermal gradients. The precisions on pressure and temperature are estimated to be ±0·02 kbar and ±5°C, respectively. High-temperature experiments (1000 and 950°C) were performed with a fast-quench device (Roux & Lefèvre, 1992) to prevent quench crystallization. The $fO_2$ of $H_2O$-saturated charges was calculated using $fH_2$ from the membrane, assuming that the fluid was pure $H_2O$, and using the $H_2O$ fugacity tables of Burnham *et al*. (1969) together with standard thermodynamic properties from Robie *et al*. (1979) for the dissociation reaction of $H_2O$ at 1 bar. Knowing the $fH_2$ and the $XH_2O^{in}$, the $fO_2$ of the $H_2O$-undersaturated charges was calculated using the following equation: $\log fO_2 = \log fO_2(a_{H2O} = 1) + 2 \log XH_2O^{in}$ (see Scaillet & Evans, 1999). The quality of $fO_2$ control was evaluated by comparing membrane-derived $fO_2$ values with those calculated using Fe–Ti oxide equilibrium, when good analyses were available. For the 880°C run, the formulation of Ghiorso & Sack (1991) gives 880°C and $\Delta$NNO = + 0·26 (where NNO is the nickel–nickel oxide buffer), which is close to the $\Delta$NNO + 0·41 given by the membrane. In membrane monitored runs, we thus consider $fO_2$ to be known within 0·15 log units. In runs at 4 kbar and 950–1000°C, $fO_2$ can only be estimated via Fe–Ti oxides. Although the formulation of Ghiorso & Sack (1991) is not calibrated for high $fO_2$, a graphical estimation (Ghiorso & Sack, 1991, fig. 4) suggests that $fO_2$ was above NNO + 2·5 in the high-temperature runs as well as one experiment at 2 kbar and 850°C performed in the IHPV 'Basset'.

Mounted charges were examined using a petrographic microscope and were then carefully analysed using a scanning electron microscope equipped with EDS (JEOL-JSM 6400) at ESEM (Université d'Orléans) to identify the mineral assemblages. Quantitative analyses of the experimental glasses (defocused beam between 5 and 10 µm) and minerals (focused beam of 1 µm) were obtained using a CAMECA SX-50 electron microprobe at the Service commun BRGM–CNRS d'Orléans, operating at 15 kV and 6 nA with a counting time of 10 s. During each analytical session, dacite to rhyolite glass standards with known $H_2O$ contents (0–9 wt %) were analysed to correct for alkali migration and to determine the $H_2O^{glass}$ of the charges using the difference to 100% method. The precision of this method is ±0·5 wt % $H_2O$ (Devine *et al*., 1995).

Several lines of evidence suggest that the experiments closely approached equilibrium (e.g. Clemens *et al*., 1986; Dall'Agnol *et al*., 1999): (1) melts and minerals with euhedral shape are homogeneously distributed across the charges; (2) their compositions are homogeneous both at grain–melt pool and charge scale, and show progressive variations with experimental parameters; (3) $T$–$fO_2$ values calculated with the experimental Fe–Ti oxides using the calibration of Ghiorso & Sack (1991) agree with the conditions imposed during the experiments (see 'Experimental and Analytical Procedures'); (4) calculated concentration ratios between coexisting phases [$(Fe/Mg)^{clinopyroxene}/(Fe/Mg)^{melt}$, $(Ca/Na)^{plagioclase}/(Ca/Na)^{melt}$] are similar to those established in other experimental studies, as detailed below.

## RESULTS

### Phase diagram at 4 kbar

Experimental results at 4 kbar are given in Tables 2 (sample 98N50) and 3 (sample 98N06). The related phase diagrams are illustrated in Fig. 4. In addition to glass and fluid phases (except in $CO_2$-free charges undersaturated in $H_2O$), the following minerals were observed:

clinopyroxene, low-Ca pyroxene (either orthopyroxene or pigeonite), amphibole, biotite, plagioclase, magnetite, ilmenite, apatite. Anhedral zircon was locally observed but its habit suggests it is actually a refractory mineral incompletely melted during the preparation of the starting material. The solidus shown corresponds to that of the haplogranite system as residual liquids trend toward this composition (Holtz & Johannes, 1994). $H_2O$ solubility varies between 8·1 and 8·8 wt % for 98N06 and between 8·2 and 9·7 wt % for 98N50. These results are in good agreement with the $H_2O$ solubility calculated using the method of Burnham (1979), except at high temperature for sample 98N50 (dotted line in Fig. 4). The liquidus was not reached in our experiments but is slightly over 1000°C at $a_{H2O} = 1$, as indicated by the low mineral proportions at this temperature and $H_2O$ content (Tables 2 and 3: 96% of glass in 98N06 and 92% of glass in 98N50).

Magnetite, ilmenite and apatite are the liquidus minerals and crystallize at temperatures slightly above 1000°C at $H_2O$-saturation. The slope of the saturation curve for the Fe–Ti oxides is not constrained by our experiments but inferred from other experimental studies (e.g. Dall'Agnol *et al*., 1999). Clinopyroxene is the first silicate to crystallize ($T > 950$°C) and is present in all charges except at low temperature ($T < 850$°C at $a_{H2O} = 1$, Cpx-out curve) for the bulk composition 98N50, in which it reacts with melt to produce amphibole. Its crystallization temperature decreases as $a_{H2O}$ increases. Plagioclase was the only tectosilicate obtained under the investigated conditions. Its crystallization temperature is very sensitive to $H_2O^{melt}$: it is a near-liquidus mineral for low $H_2O$ content in the melt ($H_2O^{melt} < 3$ wt %), and its crystallization temperature is lower than 750°C for $H_2O$-saturated conditions. Quartz and alkali feldspar were not observed in any of our experimental charges. This is not surprising, as experimental studies (e.g. Klimm *et al*., 2003) have shown that these minerals crystallize close to the solidus whereas our charges equilibrated at our lowest investigated temperature (775°C) and with the lowest $H_2O$ content in melt still contain 51 and 59 wt % glass (charges 50-31 and 06-32, respectively; Tables 2 and 3). Quartz and alkali feldspar certainly crystallize at lower temperatures and/or $H_2O$ contents than those investigated here, in agreement with petrographic observations (see above). The Low-Ca pyroxene (Lpx) stability field encompasses a large interval of temperature but is restricted to $H_2O^{melt} < 6·5$ wt % for 98N50 and < 5·2 wt % for 98N06. Because of lack of data for $T < 830$°C at low $H_2O^{melt}$, we cannot specify whether Lpx is stable at lower temperature or if it is in reaction relation with the liquid as temperature decreases (e.g. Lpx + $\text{liquid}_1 \rightarrow$ Biotite + $\text{liquid}_2$), as suggested by the dashed line in Fig. 4. The maximum crystallization temperature for amphibole is probably slightly above 880°C and its stability field is restricted to $H_2O^{melt} > 5$ wt % for sample 98N50 and $H_2O^{melt} > 6$ wt % for sample 98N06. This topology has previously been observed in experimental studies of granodioritic and granitic compositions (e.g. Naney, 1983; Dall'Agnol *et al*., 1999; Costa *et al*., 2004). The biotite stability field is very sensitive to the magma composition: its saturation curve has a weak positive slope in the phase diagram of sample 98N06, with an upper $T$ stability above 880°C. In contrast, in sample 98N50, biotite crystallizes at 860°C close to the solidus, down to below 775°C at $H_2O$ saturation; the biotite-in curve thus has a negative curvature in the $T$–$H_2O$ projection (Fig. 4).

## Experiments at 2 kbar

Two additional experiments were performed at 2 kbar and 850°C at two $fO_2$ values [~ NNO + 1·5 (Gros Bleu pressure vessel) and > NNO + 2·5 (Basset pressure vessel), Tables 2 and 3]. The aim of these experiments was to investigate the effect of pressure on the mineral stability fields, in particular that of plagioclase (see below), and the liquid line of descent. We observed the same minerals as at 4 kbar, except that no low-Ca pyroxene crystallized. The lack of low-Ca pyroxenes is probably linked to the more oxidized conditions imposed in these experiments at 2 kbar. Indeed, the experiments of Dall'Agnol *et al.* (1999) and Martel *et al.* (1999) at different $fO_2$ showed the shrinking of the low-Ca pyroxene stability field as $fO_2$ increases. Another difference between the two investigated pressures is the absence of amphibole at 2 kbar in the 98N06 composition. Either the amphibole is no longer stable in this composition at 2 kbar or it crystallizes below 850°C. In 98N50, below 3·4 wt % $H_2O$ in the melt, amphibole is replaced by clinopyroxene. Finally, the results for the 98N06 sample show that the crystallization temperature for clinopyroxene decreases with increasing $fO_2$: it is absent in the experiment at $fO_2$ > NNO + 2·5 whereas it crystallized at $fO_2$ = NNO + 1·5.

**Proportions and compositions of minerals**
Individual mineral phases in our crystallization experiments are homogeneous and the reported compositions (Tables 4–9) are considered representative of those present in a given experimental charge. Phase proportions were determined by mass balance, using the least-squares method (Tables 2 and 3).The sums of the squares of residuals are generally low ($\sum r^2 < 0{\cdot}35$).

*Fe–Ti oxides*
Fe–Ti oxides obtained in our experiments are titanomagnetites and hemoilmenites. Representative analyses of experimental Fe–Ti oxides are given in Table 4. The fractions of ulvöspinel in magnetite ($X_{\mathrm{Usp}}$) and of ilmenite in hemoilmenite ($X_{\mathrm{Ilm}}$) were calculated after Stormer (1983). Magnetite and ilmenite form large cubic–octahedral and elongated crystals in $H_2O$-saturated charges, respectively, but their sizes quickly decrease with decreasing $H_2O^{\mathrm{melt}}$. Ilmenite analyses are often contaminated by glass.

For runs at 4 kbar between 880 and 775°C, $X_{\mathrm{Usp}}$ ranges between 0·21 and 0·43 and $X_{\mathrm{Ilm}}$ ranges between 0·87 and 0·95. The $X_{\mathrm{Usp}}$ increases slightly with decreasing $H_2O^{\mathrm{melt}}$ (e.g. at 880°C, $X_{\mathrm{Usp}}$ varies between 0·36 to 0·44 for $H_2O^{\mathrm{melt}}$ between 8·2 and 4·6 wt %, respectively) as a result of the lowering of $fO_2$ with lowering $fH_2O$. $X_{\mathrm{Usp}}$ also decreases with decreasing temperature as expected (Verhoogen, 1962; Ghiorso & Sack, 1991). At 950–1000°C, the ilmenite and ulvöspinel contents are markedly lower ($X_{\mathrm{Usp}}$ <0·15 and $X_{\mathrm{Ilm}}$ <0·50), because of the more oxidizing conditions.

*Plagioclase*
The compositions of experimental and natural plagioclases are given in Table 5. Plagioclase crystallizing in both starting materials is similar at a given $T$ and $H_2O$. Its anorthite content varies between $An_{51}$ and $An_{28}$, decreasing with decreasing $T$ and $H_2O^{\mathrm{melt}}$. It partly overlaps the range displayed by the natural plagioclases but the latter are slightly more sodic ($An_{34–22}$). This slight discrepancy is interpreted as due to subsolidus re-equilibration of the natural feldspars as textural observations suggest (e.g. presence of myrmekite).

Ca–Na exchange between plagioclase and melt ($K_d$) varies between 1·45 and 3·19 in the investigated pressure range, without any obvious correlation with $H_2O^{\mathrm{melt}}$ (which varies between 3·4 and 7·8 wt %). These observations are in agreement with calculated $K_d$ values for other magmas of intermediate compositions under similar $P$–$T$–$fO_2$ conditions (2–4 kbar, NNO or NNO + 2·5). For example, the $K_d$ calculated for the Pinatubo dacite (Prouteau, 1999; Scaillet & Evans, 1999) ranges between 1·76 and 3·94 ($H_2O^{\mathrm{melt}}$ 5·0–8·5 wt %) and that for the Mt. Pelée andesites (Martel *et al.*, 1999) ranges between 2·05 and 4·71 ($H_2O^{\mathrm{melt}}$ 4·8–7·6 wt %). As in our Lyngdal experiments, for both Pinatubo and Mt. Pelée compositions, no clear correlation between the $H_2O$ content in the silicate melt and the $K_d$ is observed. This contrasts with the experiments of Sisson & Grove (1993) on high-Al basalts and low-$SiO_2$ rhyolites, in which $K_d$ increases from ~1·7 to 5·5 for 2–6 wt % $H_2O^{melt}$, respectively. We suggest that the $K_d$ sensitivity to $H_2O^{melt}$ decreases with the lowering of the Ca/Na ratio in the melt. Indeed, the majority of experimental melts from Sisson & Grove (1993)✚ have a molar ratio of $(Ca/Na)^{melt} > 1$ whereas the experiments on intermediate rocks have a $(Ca/Na)^{melt} < 1$.

Lastly, it is important to note that the difference in experimental plagioclase compositions between the Lyngdal granodiorite ($An_{51–28}$) and Pinatubo ($An_{62–30}$) or Mt. Pelée ($An_{81–55}$) is not due to different $H_2O$ contents or bulk Ca/Na ratios (0·98 for the Mt. Pelée andesite and 0·94 for sample 98N50; 0·59 for sample 98N06 and 0·60 for the Pinatubo dacite). It rather reflects the important differences in plagioclase crystallization temperature in these compositions (see below).

### *Amphibole and biotite*

In Tables 6 and 7, experimental amphiboles and biotites are compared with the natural mineral compositions. The experimental amphiboles are calcic (hornblendes *sensu lato*) and usually occur as very large euhedral crystals (up to 300 µm) containing small Fe–Ti oxide inclusions. Amphiboles that crystallized from the 98N50 and 98N06 starting products are very similar in composition for a given $H_2O^{melt}$ and $T$. The Al content is relatively constant: it varies between 1·67 to 2·03 cations p.f.u. at 4 kbar and between 1·38 and 1·75 cations p.f.u. at 2 kbar. In contrast, $X_{Fe}$ varies with temperature and $H_2O^{melt}$. At $H_2O$-saturated conditions, $X_{Fe}$ increases from 0·38 at 880°C to 0·58 at 775°C. Variations in $H_2O^{melt}$ have a smaller effect on $X_{Fe}$; for example, at 830°C, the $X_{Fe}$ of amphibole crystallizing from 98N50 varies from 0·48 (8·3 wt % $H_2O$) to 0·62 (6·5 wt % $H_2O$). This evolution of $X_{Fe}$ is mainly due to the lowering of the mg-number of the melt with decreasing $T$ and $H_2O^{melt}$. The influence of $fO_2$ on $X_{Fe}$ is examined below.

As for the amphiboles, the $X_{Fe}$ in experimental biotites ranges between 0·39 and 0·63 at 4 kbar, as a result of the effect of $H_2O^{melt}$ and temperature. Table 7 shows that the compositions of the natural biotites are well reproduced by our experiments, in terms of their Fe/Mg ratio. The experimental biotites are, however, richer in $Al_2O_3$ and $TiO_2$ and poorer in $K_2O$. The difference in the halogen contents between the experimental and natural biotites and amphiboles could be due to their partial volatilization during atmospheric melting of the samples or to the presence of an $H_2O–CO_2$ fluid in our experiments.

### *Pyroxenes*

The compositions of the experimental clinopyroxenes are given in Table 8 and can be compared with the composition of the natural clinopyroxenes. The calculated $K_d^{Fe–Mg} = [Fe/Mg]^{cpx}/[Fe/Mg]^{melt}$ (with all Fe as $Fe^{2+}$) for the $H_2O$-saturated charge (98N50) at 950°C is 0·23, which is close to the calculated $K_d$ for the Mt. Pelée andesite ($K_d$ = 0·25 at $a_{H2O} = 1$, 900°C and 2 kbar; Martel *et al*., 1999).

As for amphibole, the experimental clinopyroxene composition is similar in both starting materials for a given temperature and $H_2O^{melt}$. It is mainly a diopside–augite [after the nomenclature of Morimoto *et al*. (1988)], trending toward hedenbergite in 98N06. Here too, the $X_{Fe}$ ratio is a function of temperature and $H_2O^{melt}$. Under $H_2O$-saturation, $X_{Fe}$ increases from 0·38 at 880°C to 0·59 at 775°C, and at 850°C $X_{Fe}$ varies from 0·33 for 8·8 wt % $H_2O^{melt}$ to 0·56 for 3·6 wt % $H_2O^{melt}$. At low $H_2O^{melt}$, a low-Ca pyroxene (pigeonite or orthopyroxene; Table 9) crystallizes with the augite. Orthopyroxene crystallizes with a Ca-rich augite, whereas augite crystallizing with pigeonite has a lower Ca content. Calculated temperatures for coexisting pyroxenes with the QUILF program (Andersen *et al*., 1993) are between 57 and

259°C above the experimental temperatures. Such discrepancies are common in experimental studies (e.g. Vander Auwera & Longhi, 1994; Villiger *et al.*, 2004) and could be partially due to the calculation procedures used to project pyroxenes with relatively high contents of, for example, $Al_2O_3$ or $TiO_2$, in the wollastonite–enstatite–ferrosilite compositional space. Another problem is the presence of pigeonite in some runs, up to 100°C below the minimum temperature of its stability field determined by Lindsley (1983) in the system enstatite–ferrosilite–wollastonite. As we have only few data on coexisting pyroxenes, we cannot explore in details the effects of pyroxene and melt compositions on the differences between the experimental and calculated temperatures, and the possibility that the pyroxenes did not reach their equilibrium compositions in the experimental charges with low $H_2O$ contents cannot be excluded. However, the stability field for the low-Ca pyroxenes (Fig. 4) is likely to represent equilibrium conditions as it is consistent over a large temperature range (950–800°C) in our experiments and its $T$–$H_2O^{melt}$ relationships are similar to those in other experimental studies (e.g. Naney, 1983; Costa *et al.*, 2004).

The natural clinopyroxenes are well reproduced in our experiments with high $H_2O$ contents, with the exception of the higher $Al_2O_3$ content in the experimental clinopyroxenes (between 5·3 and 1·2 wt % $Al_2O_3$ in the experimental clinopyroxenes, compared with between 1·5 and 1·2 wt % in the natural ones). A possible explanation for the high $Al_2O_3$ content in some experimental clinopyroxenes arises from the observation that their $Al_2O_3$ content is strongly dependent on the activity of $Al_2O_3$ in the melt (Villiger *et al.*, 2004). A general co-variation between the $Al_2O_3$ molar fraction ($X_{Al2O3}$) in the melt and the $Al_2O_3$ content of the experimental clinopyroxenes is observed (Fig. 5). Actually, as we show below, our experimental melts are generally richer in $Al_2O_3$ than the natural liquid line of descent of the HBG suite. In charges where the $X_{Al2O3}$ values of the experimental melts are similar to those of the HBG rocks, the $Al_2O_3$ content of the experimental clinopyroxenes (1·7–1·2 wt % $Al_2O_3$) is similar to that of the natural ones.

### *Glasses*

Representative glass compositions are listed in Table 10. With increasing crystallization (lowering $T$ and $H_2O^{melt}$) the residual liquid becomes impoverished in MgO, FeO, CaO, $TiO_2$ and $Al_2O_3$, whereas $SiO_2$ and alkalis increase, in response to the precipitation of the plagioclase–pyroxenes–oxides (± amphibole) assemblage. The glass $SiO_2$ content for the 98N50 composition varies between 59 and 76 wt % at 1000°C and 800°C, respectively, and between 67 and 76 wt % for the 98N06 composition. The more evolved liquids trend toward the minimum of the haplogranite system and closely resemble metaluminous to slightly peraluminous high-silica rhyolites erupted in extensional continental settings such as the Bishop Tuff (Table 10) or the Yellowstone rhyolites (Hildreth, 1979; Hildreth *et al.*, 1991).

## CRYSTALLIZATION CONDITIONS OF THE LYNGDAL MAGMA

### $H_2O$ content

At a given pressure and $fO_2$, the crystallization sequence depends on the $H_2O$ content in the melt (Fig. 4). The following lines of evidence indicate that the natural sequence of crystallization can be reproduced experimentally only if high $H_2O^{melt}$ prevailed during the early stages of crystallization. First, the low-Ca pyroxene stability field is restricted to low $H_2O^{melt}$ ($H_2O^{melt} < 6·5$ wt % for 98N50, $H_2O^{melt} < 5$ wt % for 98N06) whereas amphibole crystallizes for $H_2O^{melt} > 5$ wt %. Petrographic study of the Lyngdal granodiorite samples shows that amphibole is stable in both compositions and is an early crystallizing mineral, whereas neither orthopyroxene nor pigeonite was observed, nor were the latter two minerals observed in any other HBG pluton studied by Vander Auwera *et al.* (2003). It appears that the

$H_2O$ content of the melt was probably above ~6 wt % during the crystallization of the Lyngdal granodiorite. Even if we suppose that a low-Ca pyroxene had crystallized in the Lyngdal magma and was later reacted out, another constraint on $H_2O^{melt}$ is provided by the scarcity of biotite in the least differentiated Lyngdal rocks (~60 wt % $SiO_2$) and its late crystallization relative to amphibole. Figure 4 shows that biotite crystallizes after amphibole when $H_2O^{melt}$ is above 5 wt % at 850°C and this is a minimum estimate. Indeed, biotite is more abundant than amphibole when they coexist with a low-Ca pyroxene, i.e. for $H_2O$ contents between 5·5 and 6·5% at 830°C (see Table 2 for phase proportions in the experimental charges), in disagreement with the petrographic observations. It is also worth noting that high $H_2O$ contents are supported by the abundance and large size of pegmatites (outcrops up to several hundred square meters with crystals reaching the metre scale) in Lyngdal intrusion and in other members of the HBG suite (Svedrup, 1960; Nogarède, 2001).

For this elevated $H_2O$ content, near-liquidus phases are Fe–Ti oxides, clinopyroxene and apatite, in accordance with petrographic observations, which also suggest that plagioclase crystallizes together with or only slightly before amphibole. The crystallization path for a bulk-rock $H_2O$ content of 5 wt %, calculated assuming closed-system behaviour and using experimental phase proportions, is shown by the thick grey curve in Fig. 4. Clearly, under these conditions, the natural sequence of crystallization is well reproduced.

### Oxygen fugacity

Oxygen fugacity exerts a strong control on the mineral composition (in particular, Fe–Ti oxide compositions and the $X_{Fe}$ of the ferromagnesian minerals), and comparison between the experimental products and the natural minerals allows us to estimate this parameter. However, natural Fe–Ti oxides typically re-equilibrate under subsolidus conditions and, therefore, cannot be used to constrain $fO_2$. In contrast, ferromagnesian silicates better preserve the redox conditions prevailing in the magma, even if they re-equilibrated down temperature to some extent. The following observations suggest that both clinopyroxene and amphibole compositions preserve magmatic conditions: (1) clinopyroxenes found as inclusions in amphibole and plagioclase are similar to each other; (2) amphibole in plagioclase has a composition close to that in the matrix. It is unlikely that minerals included in plagioclase would easily re-equilibrate by exchanging Fe and Mg with other minerals in the matrix. Tables 6–8 show that the compositions of the ferromagnesian minerals are well reproduced by our experiments at 4 kbar and NNO or NNO + 1. Admittedly, our experiments do not cover a sufficiently wide range in $fO_2$ to allow explicit constraints on the effect of this parameter on mineral compositions. Some insight can be gained, however, from the work of Dall'Agnol *et al.* (1999), who performed experiments on a compositionally similar, yet more evolved composition (Jamon granite, 71 wt % $SiO_2$; Fig. 1). In these experiments the $X_{Fe}$ of amphibole is 0·32 ± 0·03 between 850 and 775°C at NNO + 2·5 and 0·7 at 750°C and NNO – 1·5. Interestingly, the $X_{Fe}$ of amphiboles synthesized in our experiments at NNO or NNO + 1 broadly fills the compositional gap of amphiboles obtained at NNO + 2·5 and NNO – 1·5 by Dall'Agnol *et al.* (1999), suggesting that, at fixed $T$, $fO_2$ exerts a dominant control on the amphibole Fe/Mg ratio relative to the bulk composition. The fact that $X_{Fe}$ values as high as 0·70 are not found in Lyngdal amphiboles suggests an $fO_2$ higher than NNO – 1·5 for this pluton. The Al content of our experimental amphiboles is plotted against $X_{Fe}$ in Fig. 6. Amphibole crystallizing at NNO + 1·5 has a lower $X_{Fe}$ than its natural counterpart, whereas that obtained at NNO or NNO + 1 reproduces this ratio. Similarly, experimental clinopyroxene and biotite at NNO or NNO + 1 also reproduce fairly well the natural compositions (Tables 7 and 8). Altogether, these observations suggest that the Lyngdal magma crystallized at an $fO_2$ between NNO and NNO + 1.

## Pressure

The large hornblende–biotite intrusions of the HBG suite (Fig. 2) define a differentiation trend from 56 to 77 wt % $SiO_2$ (Vander Auwera *et al*., 2003). The experimental glasses at 4 kbar reproduce the natural HBG for several elements except for CaO and $Al_2O_3$, whose content are systematically higher in the experimental glasses, as illustrated for CaO in a $SiO_2$–CaO–(MgO + FeO + $TiO_2$) diagram (Fig. 7). As the HBG trend is thought to reflect fractionation of Fe–Ti oxides, clinopyroxene, plagioclase and apatite, with or without amphibole, from a magma similar in composition to sample 98N50 (Bogaerts *et al*., 2003a), this misfit requires further investigation. Two different processes could explain such a misfit: either the starting materials represent liquids slightly laden with liquidus minerals (oxides and/or pyroxene) or the experimental intensive parameters do not fully match the natural conditions. As previously discussed, accumulation of plagioclase, apatite and zircon is not supported by the available geochemical data (Bogaerts *et al*., 2003*a*, and section 'Experimental and analytical procedure') and a liquidus temperature near 1000°C for intermediate compositions is compatible with the high liquidus temperature of ferroan granites (~900°C for a bulk composition with $SiO_2$ = 71 wt %; Dall'Agnol *et al*., 1999). Moreover, the presence of accumulated liquidus minerals in the starting material would increase their proportions in the experimental charges, but not greatly modify the composition of the melt in equilibrium with plagioclase, clinopyroxene, Fe–Ti oxides, apatite and amphibole. A misfit related to an intensive parameter is thus favoured and examined below.

The modal proportions of representative experimental mineral assemblages from Tables 2 and 3 are normalized to 100% in Table 11 and, as the composition of the individual minerals has been measured, the chemical compositions of these assemblages can be calculated. The experimental mineral assemblages and individual mineral are plotted (Fig. 7) in the compositional space $SiO_2$–CaO–(MgO + FeO + $TiO_2$). Based on major element modelling by the least-squares method on natural rocks, Bogaerts *et al*. (2003*a*) calculated the mineral assemblages that have to be fractionated to produce the natural trend from quartz monzodiorite to granite in the HBG suite. This trend has been modelled in two steps, with step 1 (two possible models) starting from the least differentiated sample (56 wt % $SiO_2$) to an intermediate composition (62 wt % $SiO_2$), and step 2 starting from this latter composition to give a residual melt of ~72 wt % $SiO_2$. The modal proportions of the fractionated mineral assemblages (hereafter referred to as modelled mineral assemblages) are given in Table 11 and plotted in Fig. 7 in the compositional space $SiO_2$–CaO–(MgO + FeO + $TiO_2$) for comparison with the experimental mineral assemblages. The modal proportions of the experimental mineral assemblages (Table 11) first show that the proportion of oxides and clinopyroxene in experiments at approximately NNO and NNO + 1 is similar to the modelled mineral assemblages. This again supports our observation that, if present, the proportion of accumulated minerals is negligible. Second, the misfit between the experimental and modelled mineral assemblages at 4 kbar is due to a higher amphibole/plagioclase ratio in the former. A higher proportion of crystallized plagioclase should lower the CaO and $Al_2O_3$ content in the experimental glasses to fit with the HBG trend. The experiments conducted at 2 kbar show that plagioclase crystallizes at 850°C for $a_{H2O} = 1$, which is not the case at 4 kbar. However, despite this higher proportion of plagioclase at 2 kbar, the experimental glasses are still richer in $Al_2O_3$ and CaO than the natural HBG suite. Figure 7 shows that the CaO content of residual liquids is very sensitive to the plagioclase/Fe–Ti oxides ratio, which depends on pressure (mainly affecting plagioclase) and $fO_2$ (mainly affecting the Fe–Ti oxides). In the experimental mineral assemblages, this ratio appears too small when compared with the modelled mineral assemblages, which reproduce the HBG trend (Table 11). As mentioned above, our experiments at 4 kbar (<950°C) fit well the $fO_2$ of the Lyngdal magma, and the departure of the experimental glasses from the natural trend is probably due to an experimental pressure that is too high, producing a plagioclase/Fe–Ti oxides ratio (P/O) that is too low. In contrast, the misfit at 2 kbar is probably due to an $fO_2$ that is too high (>NNO + 1·5), thus crystallizing too much Fe–Ti oxides despite crystallization of a larger amount of plagioclase, which yields again a P/O ratio that is too low.

Based on the above considerations, we can constrain the emplacement pressure of the Lyngdal granodiorite. An emplacement pressure of 4 kbar is too high, as the melt does not crystallize enough plagioclase. At 2 kbar, the amount of plagioclase is higher; however, amphibole is not stable at 850°C in experiments on sample 98N06 while biotite crystallizes. Amphibole could be stable in this composition at temperature below 850°C but the natural sequence of crystallization indicates that amphibole crystallizes before biotite. We therefore conclude that the Lyngdal granodiorite most probably crystallized at pressures between 2 and 4 kbar.

## COMPARISON WITH OTHER EXPERIMENTAL STUDIES

All previous experiments on metaluminous ferroan granitoids (Clemens *et al*., 1986; Dall'Agnol *et al*., 1999; Klimm *et al*., 2003; see Fig. 1) focused on granitic magmas *sensu stricto* ($SiO_2$ > 71 wt %). This study is the first experimental investigation on ferroan magmas of intermediate compositions related to rapakivi granites, which both display low $Al_2O_3$ contents and high trace element contents (e.g. Zr, Nb, REE). In the following discussion, we start by comparing our phase relationships with those obtained on magmas that are more evolved, but of similar affinity (Clemens *et al*., 1986; Dall'Agnol *et al*., 1999; Klimm *et al*., 2003). We then compare the Lyngdal data with phase equilibria obtained for other intermediate magma compositions. The rationale here is (1) to illustrate common phase equilibrium features specific to metaluminous ferroan granitoids, (2) to highlight existing differences between this magma type and others generated in different tectonic settings.

The near liquidus phase assemblage (plagioclase, amphibole, pyroxenes, Fe–Ti oxides) of the ferroan calc-alkalic granites (Dall'Agnoll *et al*., 1999; Klimm *et al*., 2003) compares well with that of their less silicic counterparts investigated here. Pyroxenes are near liquidus phases and react out as temperature decreases, as observed at least for clinopyroxene in the Lyngdal granodiorite compositions. The stability field of amphibole extends to slightly lower $H_2O^{melt}$ in granite, 4·5 wt % as compared with 5·5 wt % in intermediate rocks, although in the more evolved variety (73·6 wt % $SiO_2$) amphibole is unstable (Klimm *et al*., 2003). Plagioclase is always the first tectosilicate to crystallize, followed by quartz and alkali feldspar, which both appear at temperatures lower than 700°C at $H_2O$-saturation. Altogether, the phase equilibria of granite and intermediate metaluminous ferroan, calc-alkalic to alkali-calcic magmas appear to be very similar, except of course that liquidus temperatures (*c*. 900°C) are depressed by *c*. 100°C in granite compositions relative to the less silicic varieties. This similarity in topology and the fact that residual liquids of intermediate metaluminous ferroan magmas (calc-alkalic to alkali-calcic) are nearly identical to the granites of similar affinity suggest that the latter can be obtained by differentiation from the former.

Intermediate magmas from convergent tectonic settings (andesites to dacites) typically have higher $Al_2O_3$ (>15 wt %) and CaO contents, and lower $FeO–TiO_2$ contents than the ferroan magma compositions (e.g. Pinatubo dacite and Mt. Pelée andesite: Table 1 and Fig. 1). Comparison between the phase diagrams for sample 98N50 and that of the andesite from Mt. Pelée (Lesser Antilles volcanic arc: Martel *et al*., 1999) shows that this compositional difference mostly affects the stability of plagioclase, which is an early phase in the andesite while its crystallization temperature is 100–150°C lower in the Lyngdal composition (at $a_{H2O}$

= 1). The same holds true when comparing composition 98N06 with the Pinatubo dacite (Luzon volcanic arc: Rutherford & Devine, 1996; Scaillet & Evans, 1999; Prouteau & Scaillet, 2003). Whereas both rocks have similar bulk-rock $SiO_2$ contents (respectively 65 and 64 wt %), plagioclase is on the liquidus at 4 kbar in the Pinatubo dacite (Prouteau & Scaillet, 2003), crystallizing at near 900°C at $H_2O$-saturation, whereas under similar $P$–$H_2O$ conditions the plagioclase saturation temperature is at least 125°C lower in the Lyngdal granodiorite. Obviously this difference in plagioclase stabilities between Lyngdal and arc magmas reflects the lower $Al_2O_3$ and CaO contents of the Lyngdal magma. The lower crystallization temperature of plagioclase in Lyngdal, as compared with our examples of arc magma compositions, explains its lower anorthite content for similar $H_2O^{melt}$ and Ca/Na ratios in the bulk compositions, as discussed above. When plagioclase starts crystallizing in the Lyngdal magma, the Ca/Na ratio of the melt has already decreased to <0·5 as a result of clinopyroxene crystallization, whereas in the Pinatubo dacite and Mt. Pelée andesite, plagioclase is a liquidus phase and $(Ca/Na)^{melt} \sim (Ca/Na)^{bulk–rock}$.

Finally, the Lyngdal phase equilibria can also be compared with those of the Fish Canyon Tuff (FCT in Table 1 and Fig. 1; Johnson & Rutherford, 1989*b*), which is a quartz latite erupted during the mid-Cenozoic in Colorado (USA). Its tectonic setting is still controversial, as the link between this magmatic episode and the Oligocene subduction of the Pacific plate beneath North America is not yet resolved (Bachmann *et al.*, 2002). The Fish Canyon Tuff shares some geochemical affinities with Lyngdal: both are ferroan and their MALI index $[(Na_2O + K_2O) – CaO]$ is similar (FCT is alkali-calcic and Lyngdal straddles the calc-alkaline–alkali-calcic boundary; Fig. 1). However, as for subduction zone magmas relative to Lyngdal, FCT is poorer in $TiO_2$ and $FeO_t$ and richer in $Al_2O_3$ (Table 1). At $H_2O$-saturation Lyngdal has a higher liquidus temperature (*c*. 1000°C) than FCT (*c*. 930°C). The plagioclase-in curve is much steeper in Lyndgal, inducing a lower crystallization temperature (<750°C) than in FCT (near 800°C at $a_{H2O}$ = 1) but near-liquidus crystallization in Lyngdal (>1000°C) at low $H_2O$ contents. Amphibole and biotite display similar crystallization temperatures in both compositions, although the amphibole stability field seems more restricted in Lyndgal. In the FCT composition, the crystallization temperature of amphibole is near 900°C, even for low $H_2O$ contents in the melt, and there is no low-Ca pyroxene. The difference in stability of amphibole is even more significant at lower pressure, where its crystallization temperature at $a_{H2O}$ = 1 is near 900°C for the FCT composition and lower than 850°C in Lyngdal. Moreover for the FCT composition, clinopyroxene is in peritectic reaction with hornblende near 825°C and is thus stable over a restricted temperature interval (~100°C). In the Lyngdal composition, this temperature interval is twice as large.

The above comparison shows that, although metaluminous ferroan, calc-alkalic to alkali-calcic granitoids are clearly rich in alkalis (especially $K_2O$), in terms of phase relations the key elements that readily distinguish them from intermediate magmas at convergent margins is their low contents of $Al_2O_3$ and CaO. Although this view might be considered merely the reciprocal of an alkalis–alumina balance, the phase equilibria comparison shows that metaluminous ferroan magmas should be viewed not only as alkali rich but also as $Al_2O_3$- and CaO-poor rocks (Eby, 1990). It is the actual content of both elements that controls plagioclase stability.

# DISCUSSION

## General

Many ferroan granitoids were originally believed to be anhydrous and reduced, and were termed A-type granites (Loiselle & Wones, 1979; Collins *et al*., 1982). Although these conditions of crystallization have been confirmed in some cases, for example the charnockites of Bjerkreim–Sokndal (Vander Auwera & Longhi, 1994; Duchesne & Wilmart, 1997), the experimental work of Clemens *et al*. (1986) and Klimm *et al*. (2003) has shown that ferroan granitoids from the Lachlan Fold Belt of Australia were not anhydrous, but had $H_2O$ contents similar to those of calc-alkaline magmas [$H_2O$ between 2·4 and 4·3 wt %; traditionally referred to as I-type and defined as magnesian calcic or calc-alkalic granitoids after Frost *et al*. (2001)]. These studies also confirmed the reduced nature of the Australian ferroan granitoids ($fO_2$ between FMQ – 1 and FMQ – 3, where FMQ is the fayalite–magnetite–quartz buffer). In contrast, Anderson (1983) showed that ferroan granitoids can crystallize over a large range of $fO_2$ ($fO_2$ between FMQ + 3 and FMQ – 4). This observation has been confirmed experimentally by the work of Dall'Agnol *et al*. (1999) and by the results of this study, which constrain $fO_2$ between NNO and NNO + 1 during crystallization of some ferroan granitoid magmas. These oxidized granitoids also have high $H_2O$ contents: 4·5–6·5 wt % $H_2O^{melt}$ at an early stage of crystallization of the Jamon granite (Dall'Agnol *et al*., 1999) and 5–6 wt % for the Lyngdal granodiorite. An important aspect of the present study is that the Lyngdal granodiorite extends the compositional trend of oxidized and hydrous ferroan granitoids toward less silicic compositions. These observations illustrate that ferroan granitoid magmas of intermediate composition encompass a large range of $fO_2$ and melt $H_2O$ contents, suggesting that a variety of sources are involved in the generation of ferroan magmas worldwide. We return to this point below where we discuss, in greater detail, the possible sources of the Lyngdal granodiorite.

## Origin of the Lyngdal granodiorite

We start this section by summarizing the constraints on the origin of the Lyngdal granodiorite provided by this study and that of Bogaerts *et al*. (2003*a*), who made a detailed field and geochemical study (major and trace elements, Sr–Nd isotopes) of the Lyngdal intrusion and its satellite massif (Tranevåg). The least differentiated samples from the Lyngdal and Tranevåg massifs have $SiO_2$ content around 60 and 56 wt %, respectively. Major and trace element modelling, combined with Sr–Nd isotope data, indicates that these magmas could be parental to the more evolved compositions observed in Tranevåg (up to ~72% $SiO_2$) without significant crustal contamination (Bogaerts *et al*., 2003*a*) and that the Lyngdal–Tranevåg granitoids could be produced via a simple crystal fractionation process. Our phase equilibrium constraints suggest that the Lyngdal–Tranevåg rock suite can be produced by crystal fractionation of 98N50 type magmas at 3 ± 1 kbar. The fact that the experimentally derived liquid compositions conform closely to the natural rock series suggests that the starting rock compositions selected here are good analogues of the parental magmas, which were not significantly affected by crystal accumulation during crystallization. This, together with the phase equilibrium constraints detailed above, suggests that the magma parental to the Lyngdal granodiorite was emplaced as a near liquidus body.

The formation of granitoids from nearly crystal-free melts seems to be a common process (e.g. Scaillet *et al*., 1998) and has been explained as the consequence of their rapid emplacement in the upper crust (e.g. Wall *et al*., 1987). By analogy, this suggests rapid ascent of the Lyngdal magma from its source to the emplacement level, probably via dyking (e.g. Clemens & Mawer, 1992). Density and viscosity calculations for the Lyngdal magma, based on results from this experimental study, support such a hypothesis (Bogaerts *et al.*, 2003*b*). We now address the issue of whether these intermediate magmas are derived via crustal anatexis or are the differentiated products of more mafic compositions.

*Crustal anatexis*

Figure 8 (modified after Scaillet *et al.*, 1998) illustrates the relationship between temperature and $H_2O^{melt}$ for a variety of granitic magma compositions (metaluminous, peraluminous, peralkaline) emplaced in different tectonic settings. The observed negative correlation between $T$ and $H_2O^{melt}$ can be explained by the strong buffering effect of dehydration partial melting reactions in the crust (see Clemens & Watkins, 2001), i.e. $a_{H2O}$ is fixed by the melting temperature of a given protolith. Clemens & Watkins (2001) concluded that the absence of hot and wet magmas implies fluid-absent or evolution to fluid-absent conditions during partial melting in the continental crust. Specifically, anatectic melts of andesitic–dacitic composition produced via dehydration melting of basalt sources (or their metamorphosed equivalents such as amphibolites) require melt fractions higher than 40 wt % (e.g. Rapp & Watson, 1995). At such high melt fractions, the melt $H_2O$ content is unlikely to exceed 3 wt %. In contrast, our results show that the Lyngdal granodiorite crystallized from a hydrous and hot magma that clearly plots off the main trend (Fig. 8). Therefore, assuming that the emplacement conditions of the Lyngdal granodiorite are well constrained, two hypotheses can explain this off-trend position: (1) the magma formed by fluid-present melting; (2) the magma is the differentiation product of a more mafic composition, the high $H_2O$ content resulting from the incompatible character of this component in the mafic magma. Fluid-present melting of lower crustal (i.e. andesitic to basaltic) lithologies is unlikely to yield $Al_2O_3$- and CaO-poor anatectic melts, as many experimental studies have shown (e.g. Beard & Lofgren, 1991), because excess $H_2O$ promotes extensive melting of plagioclase in the protolith, giving rise to tonalitic magmas. Also, it seems difficult to have fluid-present conditions during the whole interval of crustal fusion (see Clemens & Vielzeuf, 1987), in particular when a high degree of partial melting and high magma volumes are required to produce partial melts of andesitic–dacitic composition, as is the case for the Lyngdal granodiorite and other HBG plutons in southern Norway. The second hypothesis is thus preferred and examined below.

*Fractionation from a mafic magma*

The origin of the coeval charnockitic magma belonging to the AMC suite of the Rogaland Intrusive Complex is well constrained and is compared here with possible interpretations on the origin of the HBG suite. Charnockites of the Bjerkreim–Sokndal massif are mainly explained as the differentiation products of a jotunitic (hypersthene monzodiorite) parental magma; however, Vander Auwera *et al.* (1998) did not exclude the possibility of deriving some quartz mangerites by partial melting of the lower crust. These rocks display a continuous liquid line of descent variably affected by crustal assimilation (Wilmart *et al.*, 1989; Duchesne & Wilmart, 1997; Bolle *et al.*, 2003). Experimental studies and mineral compositional data (Vander Auwera & Longhi, 1994; Duchesne & Wilmart, 1997) indicate that these magmas crystallized at an $fO_2$ between FMQ and FMQ – 1 and under relatively dry conditions ($a_{H2O}$ increased to 0·3 in the most differentiated charnockites). The feasibility of a jotunitic parent magma for the Lyngdal granodiorite is examined below.

Based on REE modelling, Duchesne & Demaiffe (1978) proposed that the Lyngdal granodiorite could represent a residual melt from the crystallization of a jotunitic parent magma. The difference in $fO_2$ (between FMQ or FMQ – 1 for the jotunite and NNO or NNO + 1 for the Lyngdal granodiorite) could be explained by crustal assimilation. Such a contamination process is considered important in explaining differences in composition and

$fO_2$ between various granitoids in the Laramie complex (Anderson *et al*., 2003). Anderson *et al*. observed that the Red Mountain Pluton, which exhibits the most extreme ferroan geochemistry, i.e. very high $FeO_t/(FeO_t + MgO)$ ratios, but also very high $K_2O$ and REE–HFSE (high field strength element) contents, is also the most reduced and least contaminated magma type of the Laramie complex. Its differentiation trend on a $T$–$fO_2$ diagram is shown in Fig. 9. The less extreme ferroan character of other granitoids from the same magmatic suite (e.g. the Sherman batholith), in particular their higher $fO_2$ (Fig. 9) was attributed by those workers to crustal assimilation. Anderson *et al*. (2003) concluded that the ferroan plutons of the Laramie complex are differentiates or partial melts of underplated tholeiitic magmas [the 'tholeiitic connection' of Frost & Frost (1997)], variably contaminated by felsic crust, and they suggested that this model could explain the variability of ferroan granitoids worldwide. In southern Norway, the situation appears different. As previously noted, the AMC suite is produced by the crystallization of primitive jotunites variably contaminated by the gneissic basement of the Rogaland–Vest Agder sectors (Bolle *et al*., 2003). As observed in Fig. 10, crustal contamination appears to be important for the petrogenesis of the charnockites, but they nevertheless preserve the dry and reduced character of their jotunitic parent magma (Duchesne & Wilmart, 1997; Vander Auwera *et al*., 1998). In contrast, the HBG suite exhibits a larger variation in $^{143}Nd/^{144}Nd$ calculated at 950 Ma, expressed in $\varepsilon_{Nd}$ values in Fig. 10 (–0·4 to –4·63) for a small variation of initial $^{87}Sr/^{86}Sr$ ratios (0·7038–0·7058), implying a different crustal contaminant if we admit that the HBG suite is also derived from a jotunitic parent magma. A different crustal contaminant could explain the higher $fO_2$ and the high $H_2O$ contents of the HBG suite. However, this model does not explain the similar isotopic compositions of the Lyngdal granodiorite and some of the evolved jotunites, which partly overlap (around $\varepsilon_{Nd} = -1$ and $^{87}Sr/^{86}Sr = 0·7057$; Fig. 10). If both magmatic suites were derived from the same parent magma, this overlap suggests that they were contaminated by a similar component consisting of a mixture of the two extreme crustal end-members. This is in contradiction to their strong differences in $fO_2$ and $H_2O$ contents. Moreover, if the HBG suite results from mixing between a jotunitic magma (and its derivates) and an $H_2O$-rich contaminant, we would expect a large variation in $H_2O$ content among the plutons forming the HBG suite, producing different facies: opx- and biotite-rich to amphibole-rich assemblages. Our phase diagrams do indeed show that variations in $H_2O$ content produce differences in the nature and amount of the ferromagnesian minerals. However, all the HBG plutons have the same mineral assemblage and mineral compositions. These observations strongly suggest that the AMC and HBG suites have different parent magmas, even if an origin from similar magmas contaminated by different crustal components cannot be completely ruled out.

The Lyngdal granodiorite and the Tranevåg massif (and the HBG suite in general) define similar, but distinct major element compositional trends compared with the AMC suite (Vander Auwera *et al*., 2001; Fig. 1). Vander Auwera *et al*. (2003) studied small mafic–intermediate massifs (Handeland and Åseral intrusions) associated with the hornblende–biotite granitoids of the HBG suite, and also considered small contemporaneous gabbronorite massifs (Demaiffe *et al*., 1990) cropping out near the Lyngdal granodiorite. They suggested the possible existence of a liquid line of descent from gabbronorites to the quartz monzodiorites–granodiorites in the lower crust. The gabbronorites have geochemical similarities to the jotunites but could be more oxidized and hydrous (Vander Auwera *et al*., 2003) and could thus represent potential parent magmas to the HBG suite. Testing this hypothesis is beyond the scope of the present study; however, the important point to stress here is that this model is very similar to that proposed for the Mesoproterozoic (1600–1300 Ma) ferroan granitoids of Laurentia and Baltica by Anderson & Morrison (2005). Those workers proposed that the oxidized or reduced nature of the granitoids in this magmatic province is due to the composition of the lower crust, i.e. that the $fO_2$ of a magma is a probe for the $fO_2$ of its source (Carmichael, 1991).

## Comparison with volcanic rocks

Frost & Frost (1997) have emphasized the compositional similarities between reduced ferroan granites and some recently erupted rhyolites such as those from Yellowstone. In the following discussion, we show that some extrusive rocks do indeed compare well with ferroan granitoids similar to those investigated here or to their expected derivatives.

High-silica rhyolites can be derived by partial melting of, or by differentiation from, more mafic magmas. The latter model is well illustrated by our crystallization experiments, which produce high-silica melts. Table 10 shows the compositional convergence of the glasses produced by the Fish Canyon Tuff (FCT) and Lyngdal experiments (4 kbar, $T$ < 850°C) as well as their resemblance to natural high-silica rhyolites such as the Bishop Tuff. As previously noted, these experimental melts are in equilibrium with different mineral assemblages for similar intensive parameters. This reflects their crystallization on different cotectic curves converging towards the haplogranite minimum and underlines the importance of bulk-rock composition on the mineral assemblage in equilibrium with the rhyolitic melt. Pre-eruptive conditions for the pyroxene-bearing facies of the Bishop Tuff (quartz, sanidine, plagioclase, biotite, ilmenite, magnetite, apatite, zircon, and augite plus orthopyroxene: Hildreth, 1979) have been estimated at: $T$ between 800 and 850°C, $H_2O^{melt}$ between 3·5 and 5·5 wt %, $fO_2$ between NNO + 0·3 and NNO + 0·6, and pressure at 2·7 ± 0·6 kbar (mineral and fluid inclusion data: Frost & Lindsley, 1992; Anderson *et al*., 2000). Our lowest $T$ and $H_2O^{melt}$ experiments approach these conditions (Fig. 4) and the mineral assemblage and composition of the Bishop Tuff are relatively well reproduced by our experiments at the lowest temperature and $H_2O$ contents (Tables 4–10), which are probably not very far from quartz and K-feldspar saturation. Observing that the silica content of extra-caldera volcanic rocks decreases with time from ~75 to 64 wt % $SiO_2$, Bailey *et al*. (1976) suggested that the high-silica rhyolites could be fractionated products from an intermediate parent magma. Based on the previous discussion, a magma similar to the Lyngdal granodiorite, although probably with a lower initial $H_2O^{melt}$, could represent such a parental magma to the Bishop Tuff. Thus, as for their reduced counterparts, the comparison of the silicic derivatives obtained in the present study with volcanic rocks shows that some moderately oxidized high-silica rhyolites can be derived by crystallization of intermediate, metaluminous, ferroan magmas.

Finally, as shown in Table 1, it is worth noting that the composition of the Lyngdal granodiorite is similar to that of the abundant quartz latites from the Etendeka and Paraná provinces of Namibia and Brazil (Fig. 1), which were erupted at *c*. 132 Ma and contain phenocrysts of plagioclase, pyroxenes (pigeonite ± augite, pigeonite ± hypersthene) and titanomagnetite (Ewart *et al*., 1998, 2004). These voluminous silicic volcanic successions have been interpreted as the extrusive equivalents of igneous ferroan charnockites (Kilpatrick & Ellis, 1992), formed via melting of a previously dehydrated crustal granulite source. They are associated with flood basalts erupted during the early Cretaceous rifting of the Africa–South America supercontinent, which led to the opening of the South Atlantic Ocean. Thus their tectonic context is extensional. The phase diagram for 98N06 shows that the Etendeka mineral assemblage can be produced at high temperatures (~1000°C), in agreement with estimated crystallization temperatures of 1000–1100°C, deduced from pyroxene equilibria in the quartz latites (Ewart *et al*., 1998). The presence of pigeonite also confirms that the anhydrous phenocryst assemblage reflects the low $H_2O$ content of the Etendeka–Paraná quartz latite magmas rather than only their high temperature. The dry character is matched by the evolution of the magmas at low $fO_2$ (below FMQ), which is in contrast to the more oxidized nature of the Lyngdal magma. In this respect, the $T$–$fO_2$–$H_2O$ conditions inferred for the Etendeka rocks are similar to those of the quartz mangerites and charnockites of the Bjerkreim–Sokndal massif of the Rogaland anorthositic province. However, the latter are interpreted to be mainly derived from the differentiation of a dry and reduced jotunitic parent magma (e.g. Duchesne & Wilmart, 1997; Vander Auwera *et al*., 1998), whereas geochemical modelling has shown that, although coeval with flood basalts, the Etendeka latites are more likely to be mainly derived from lower crustal melting (Ewart *et al*., 1998). Thus, despite similar bulk-rock compositions, metaluminous ferroan magmas of intermediate composition appear to display a large range of $H_2O$ contents and $fO_2$: from hydrous and oxidized (Lyngdal), to $H_2O$-poor and reduced (Etendeka–Paraná quartz latites). The probable parental magma to the Bishop Tuff should have crystallization conditions intermediate between these two end-member types. This diversity in crystallization conditions for intermediate metaluminous ferroan volcanic rocks is thus similar to that inferred for the related ferroan plutons.

The multiplicity of petrogenetic schemes proposed for such magmas illustrates the great variability of metaluminous ferroan magmas, showing that no single model is of wider applicability than any other. The points we want to stress here are that: (1) the occurrence of Cretaceous volcanic rocks with similar compositions to the magmas of southern Norway shows that intermediate ferroan magmas are not restricted to the Proterozoic (e.g. Frost & Frost, 1997; Eby, 1990); (2) the comparison between the Lyngdal granodiorite, Rogaland quartz mangerites and Etendeka quartz latites shows their almost identical composition in terms of major elements (Table 1), yet each has, apparently, a different origin. This is a remarkable feature, which shows that no single model is of wider applicability than any other.

## CONCLUSIONS

Our experimental study on the Lyngdal granodiorite leads us to the following conclusions. The Lyngdal granodiorite was emplaced between 2 and 4 kbar as a near liquidus melt at ~ 1000°C. This magma was relatively oxidized ($fO_2$ between NNO and NNO + 1) with a high $H_2O$ content (5–6 wt % $H_2O$ at an early stage of crystallization). These attributes sharply contrast with the dry and reduced ($fO_2$ < NNO – 1) character of the felsic magmas (quartz mangerites and charnockites) of the coeval Rogaland anorthositic complex (AMC suite). The very high $H_2O$ content of the Lyngdal magma and its liquidus temperature near 1000°C suggest that it was produced by the differentiation of a mafic melt rather than directly produced by dehydration melting in the lower crust. This parent magma composition could be similar to that of the gabbronorites cropping out north of the Lyngdal granodiorite, which locally mingled with it (Bogaerts *et al*., 2003*a*; Vander Auwera *et al*., 2003).

The comparison with other calc-alkalic to alkali-calcic, metaluminous ferroan intermediate magmas, such as the quartz latites from the Etendeka–Paraná Province, shows that intermediate, metaluminous ferroan magmas with similar anhydrous compositions have been erupted in the recent past. Our study underlines the range of variation of crystallization conditions, from anhydrous and reduced to oxidized and hydrous. This implies a great variety of sources able to produce this type of magma. Oxidized metaluminous ferroan granites can be generated via differentiation of magmas similar to the Lyngdal granodiorites (possibly with variable $H_2O$ contents) or by partial melting of a lower oxidized crust.

## ACKNOWLEDGEMENTS

M.B. thanks the Belgian FNRS for having funded this research (FRIA grant between 1998 and 2000 and 'Mandat d'Aspirant du FNRS' between 2000 and 2002) and a travel grant (Bourse de voyage) from the Communauté française de Belgique. R. Champallier, F. Gaillard and O. Rouer are thanked for their help during the experiments and microprobe analyses. Reviews by E. Anthony, B. Bonin, B. R. Frost and E. W. Hildreth helped to improve the manuscript. The editorial handling by M. Wilson is greatly appreciated.

## REFERENCES

Andersen D. J., Lindsley D. H., Davidson P. M. (1993) QUILF: a PASCAL program to assess equilibria among Fe–Mg–Mn–Ti oxides, pyroxenes, olivine and quartz. *Computers and Geosciences* **19:**1333–1350.

Andersen T., Andresen A., Sylvester A. G. (2002) Timing of late- to post-tectonic Sveconorwegian granitic magmatism in South Norway. *Norges Geologiske Undersøkelse Bulletin* **440:**5–18.

Anderson A. T., Davis A. M., Lu F. (2000) Evolution of Bishop Tuff rhyolitic magma based on melt and magnetite inclusions and zoned phenocrysts. *Journal of Petrology* **41:**449–473.

Anderson C. I., Frost C. D., Frost B. R. (2003) Petrogenesis of the Red Mountain pluton, Laramie anorthosite complex, Wyoming: implications for the origin of A-type granite. *Precambrian Research* **124:**243–267.

Anderson J. L. (1983) Proterozoic anorogenic granite plutonism of North America. In Medaris L. G., Byers C. W. J., Mickelson D. M., Shanks W. C. (Eds.). Proterozoic Geology: Selected Papers from an International Proterozoic Symposium. Geological Society of America, Memoirs **162:** pp. 133–154.

Anderson J. L. and Bender E. E. (1989) Nature and origin of Proterozoic A-type granitic magmatism in the southwestern United States of America. *Lithos* **23:**19–52.

Anderson J. L. and Morrison J. (2005) Ilmenite, magnetite, and peraluminous Mesoproterozoic anorogenic granites of Laurentia and Baltica. *Lithos* **80:**45–60.

Bachmann O., Dungan M. A., Lipman P. W. (2002) The Fish Canyon magma body, San Juan Volcanic Field, Colorado: rejuvenation and eruption of an upper-crustal batholith. *Journal of Petrology* **43:**1469–1503.

Bailey R. A., Dalrymple G. B., Lanphere M. A. (1976) Volcanism, structure, and geochronology of Long Valley caldera, Mono County, California. *Journal of Geophysical Research* **81:**725–744.

Barbey P., Nachit H., Pons J. (2001) Magma–host interactions during differentiation and emplacement of a shallow-level, zoned granitic pluton (Tarçouate pluton, Morocco): implications for magma emplacement. *Lithos* **58:**125–143.

Beard J. S. and Lofgren G. E. (1991) Dehydration melting and water-saturated melting of basaltic and andesitic greenstones and amphibolites at 1, 3, 6, 9 kbar. *Journal of Petrology* **32:**365–401.

Bellieni G., Comin-Chiaramonti P., Marques L. S., Melfi A., Nardy A. J. R., Papatrechas C., Piccirillo E. M., Roisenberg A., Stolfa D. (1986) Petrogenetic aspects of acid and basic lavas from the Parana Plateau (Brazil): mineralogical and petrochemical relationships. *Journal of Petrology* **27:**915–944.

Bingen B. and Stein H. J. (2003) Molybdenite Re–Os dating of biotite dehydration melting in the Rogaland high-temperature granulites, S Norway. *Earth and Planetary Science Letters* **208:**181–195.

Bingen B. and van Breemen O. (1998) U–Pb monazite ages in amphibolite- to granulite-facies orthogneiss reflect hydrous mineral breakdown reactions: Sveconorwegian Province of SW Norway. *Contributions to Mineralogy and Petrology* **132:**336–353.

Bingen B., Birkeland A., Nordgulen Ø., Sigmond E. M. O. (2001) Correlation of supracrustal sequences and origin of terranes in the Sveconorwegian orogen of SW Scandinavia: SIMS data on zircon in clastic metasediments. *Precambrian Research* **108:**293–318.

Bingen B., Skår Ø., Marker M., Sigmond E. M. O., Nordgulen Ø., Ragnhildstveit J., Mansfeld J., Tucker R. D., Liégeois J.-P. (2005) Timing of continental building on the Sveconorwegian orogen, SW Scandinavia. *Norwegian Journal of Geology* **84:**87–116.

Bingen B., Stein H. J., Bogaerts M., Bolle O., Mansfeld J. (2006) Molybdenite Re–Os dating constrains late-orogenic gneiss formation in the Sveconorwegian orogen, SW Scandinavia. *Lithos* **87:**328–356;

Bogaerts M., Scaillet B., Liégeois J.-P., Vander Auwera J. (2003a) Petrology and geochemistry of the Lyngdal granodiorite (Southern Norway) and the role of fractional crystallization in the genesis of Proterozoic ferro-potassic A-type granites. *Precambrian Research* **124:**149–184.

Bogaerts M., Scaillet B., Vander Auwera J. (2003b) Emplacement of the Lyngdal granodiorite (SW Norway) at the brittle–ductile transition in a hot crust. *Geophysical Research Abstracts* **5:**.

Bolle O., Demaiffe D., Duchesne J.-C. (2003) Petrogenesis of jotunitic and acidic members of an AMC suite (Rogaland anorthosite province, SW Norway): a Sr and Nd isotopic assessment. *Precambrian Research* **124:**185–214.

Burnham C. W. (1979) The importance of volatile constituents. In Yoder H. S. (Ed.). The Evolution of the Igneous Rocks: Fiftieth Anniversary Perspectives(Princeton University Press, Princeton, NJ) pp. 439–482.

Burnham C. W., Holloway J. R., Davis N. F. (1969) Thermodynamic properties of water to 1000°C and 10 000 bars. *Geological Society of America, Special Papers* **132:**1–96.

Carmichael I. S. E. (1991) The redox states of basic and silicic magmas: a reflection of their source region? *Contributions to Mineralogy and Petrology* **106:**129–141.

Chou I. M. (1987) Oxygen buffer and hydrogen sensor technique at elevated pressures and temperature. In Barnes H. L. and Ulmer G. C. (Eds.). Hydrothermal Experimental Techniques(John Wiley, New York) pp. 61–99.

Clemens J. D. and Mawer C. K. (1992) Granitic magma transport by fracture propagation. *Tectonophysics* **204:**339–360.

Clemens J. D. and Vielzeuf D. (1987) Constraints on melting and magma production in the crust. *Earth and Planetary Science Letters* **86:**287–306.

Clemens J. D. and Watkins J. M. (2001) The fluid regime of high-temperature metamorphism during granitoid magma genesis. *Contributions to Mineralogy and Petrology* **140:**600–606.

Clemens J. D., Holloway J. R., White A. J. R. (1986) Origin of an A-type granite: experimental constraints. *American Mineralogist* **71:**317–324.

Collins W. J., Beams S. D., White A. J. R., Chappell B. W. (1982) Nature and origin of A-type granites with particular reference to southeastern Australia. *Contributions to Mineralogy and Petrology* **80:**189–200.

Costa F., Scaillet B., Pichavant M. (2004) Petrological and experimental constraints on the pre-eruptive conditions of Holocene dacite from Volcán San Pedro (36°S, Chilean Andes) and the importance of sulphur in silicic subduction-related magmas. *Journal of Petrology* **45:**855–881.

Dall'Agnol R., Scaillet B., Pichavant M. (1999) An experimental study of a lower Proterozoic A-type granite from the Eastern Amazonian Craton, Brazil. *Journal of Petrology* **40:**1673–1698.

Demaiffe D., Bingen B., Wertz P., Hertogen J. (1990) Geochemistry of the Lyngdal hyperites (S.W. Norway): comparison with the monzonorites associated with the Rogaland anorthosite complex. *Lithos* **24:**237–250.

Devine J., Gardner J. E., Brack H. P., Layne G. D., Rutherford M. J. (1995) Comparison of microanalytical methods for estimating $H_2O$ content of silicic volcanic glasses. *American Mineralogist* **80:**319–328.

Duchesne J.-C. and Demaiffe D. (1978) Trace elements and anorthosite genesis. *Earth and Planetary Science Letters* **38:**249–272.

Duchesne J.-C. and Wilmart E. (1997) Igneous charnockites and related rocks from the Bjerkreim–Sokndal layered intrusion (Southwest Norway): a jotunite (hypersthene monzodiorite)-derived A-type granitoid suite. *Journal of Petrology* **38:**337–369.

Duchesne J.-C., Maquil R., Demaiffe D. (1985) The Rogaland anorthosites: facts and speculations. In Tobi A. C. and Touret J. L. R. (Eds.). The Deep Proterozoic Crust in the North Atlantic Provinces(Reidel, Dordrecht) pp. 449–476.

Dupont A. and Vander Auwera J. (2002) Geochemistry of the Farsund charnockite (SW Norway): preliminary results. In Vander Auwera J. (Ed.). Modelling of Magma Chambers and Implications for the Evolution of the Continental Crust. Symposium in Honour of Jean-Clair DuchesneUniversité de Liège pp. 16–17.

Dupont A., Vander Auwera J., Pin C., Paquette J.-L., Bogaerts M. (2005) Inefficiency of magma mixing and source heterogeneity in the genesis of granitoids: the example of the Farsund intrusion (southern Norway). *Geophysical Research Abstracts* **7:**.

Eby G. N. (1990) The A-type granitoids: a review of their occurrence and chemical characteristics and speculations on their petrogenesis. *Lithos* **26:**115–134.

Emslie R. F. and Stirling J. A. R. (1993) Rapakivi and related granitoids of the Nain plutonic suite: geochemistry, mineral assemblages and fluid equilibria. *Canadian Mineralogist* **31:**821–847.

Emslie R. F., Hamilton M. A., Thiérault R. J. (1994) Petrogenesis of a Mid-Proterozoic Anorthosite–Mangerite–Charnockite–Granite (AMCG) complex: isotopic and chemical evidence from the Nain plutonic suite. *Journal of Geology* **103:**539–558.

Ewart A., Milner S. C., Armstrong R. A., Duncan A. R. (1998) Etendeka volcanism of the Goboboseb Mountains and Messum Igneous Complex, Namibia. Part II: voluminous quartz latite volcanism of the Awahab magma system. *Journal of Petrology* **39:**227–253.

Ewart A., Marsh J. S., Milner S. C., Duncan A. R., Kamber B. S., Armstrong R. A. (2004) Petrology and geochemistry of Early Cretaceous bimodal continental flood volcanism of the NW Etendeka, Namibia. Part 2: Characteristics and petrogenesis of the high-Ti latite and high-Ti and low-Ti voluminous quartz latite eruptives. *Journal of Petrology* **45:**107–138.

Faure G. (1986) Principles of Isotope Geology(John Wiley, New York).

Frost C. D. and Frost B. R. (1997) Reduced rapakivi-type granites: the tholeiite connection. *Geology* **25:**647–650.

Frost B. R. and Lindsley D. H. (1992) Equilibria among Fe–Ti oxides, pyroxenes, olivine, and quartz: Part II. Application. *American Mineralogist* **77:**1004–1020.

Frost C. D., Frost B. R., Chamberlain K. R., Edwards B. R. (1999) Petrogenesis of the 1·43 Ga Sherman Batholith, SE Wyoming, USA: a reduced, rapakivi-type anorogenic granite. *Journal of Petrology* **40:**1771–1802.

Frost B. R., Arculus R. J., Barnes C. G., Collins W. J., Ellis D. J., Frost C. D. (2001) A geochemical classification of granitic rock suites. *Journal of Petrology* **42:**2033–2048.

Frost C. D., Frost B. R., Bell J. M., Chamberlain K. R. (2002) The relationship between A-type granites and residual magmas from anorthosite: evidence from the northern Sherman batholith, Laramie Mountains, Wyoming, USA. *Precambrian Research* **119:**45–71.

Garland F., Hawkesworth C. J., Mantovani M. S. M. (1995) Description and petrogenesis of the Parana rhyolites, southern Brazil. *Journal of Petrology* **36:**1193–1227.

Ghiorso M. S. and Sack R. O. (1991) Fe–Ti oxide geothermometry: thermodynamic formulation and the estimation of intensive variables in silicic magmas. *Contributions to Mineralogy and Petrology* **108:**485–510.

Hildreth W. (1979) The Bishop Tuff: evidence for the origin on compositional zonation in silicic magma chambers. *Geological Society of America, Special Papers* **180:**43–75.

Hildreth W., Halliday A. N., Christiansen R. L. (1991) Isotopic and chemical evidence concerning the genesis and contamination of basaltic and rhyolitic magma beneath the Yellowstone Plateau Volcanic Field. *Journal of Petrology* **32:**63–138.

Holtz F. and Johannes W. (1994) Maximum and minimum water contents of granitic melts: implications for chemical and physical properties of ascending magmas. *Lithos* **32:**149–159.

Johansson L., Möller C., Söderlund U. (2001) Geochronology of eclogite facies metamorphism in the Sveconorwegian Province of SW Sweden. *Precambrian Research* **106:**261–275.

Johnson M. C. and Rutherford M. J. (1989a) Experimental calibration of the aluminium-in-hornblende geobarometer with application to Long Valley caldera (California) volcanic rocks. *Geology* **17:**837–841.

Johnson M. C. and Rutherford M. J. (1989b) Experimentally determined conditions in the Fish Canyon Tuff magma chamber, Colorado. *Journal of Petrology* **30:**711–737.

Kilpatrick J. A. and Ellis D. J. (1992) C-type magmas: igneous charnockites and their extrusive equivalents. *Transactions of the Royal Society of Edinburgh: Earth Sciences* **83:**155–164.

King P. L., Chappell B. W., Allen C. M., White A. J. R. (2001) Are A-type granites the high temperature felsic granites? Evidence from fractionated granites of the Wangrah Suite. *Australian Journal of Earth Sciences* **48:**501–514.

Klimm K., Holtz F., Johannes W., King P. L. (2003) Fractionation of metaluminous A-type granites: an experimental study of the Wangrah Suite, Lachlan Fold Belt, Australia. *Precambrian Research* **124:**327–341

Leake B. E. (1978) Nomenclature of amphiboles. *Canadian Mineralogist* **16:**501–520.

Leake B. E., Woolley A. R., Arps C. E. S., et al. (1997) Nomenclature of amphiboles: report of the subcommittee on amphiboles of the International Mineralogical Association, commission on new minerals and mineral names. *Canadian Mineralogist* **35:**219–246.

Lindsley D. H. (1983) Pyroxene thermometry. *American Mineralogist* **68:**477–493.

Loiselle M. C. and Wones D. R. (1979) Characteristics and origin of anorogenic granites. *Geological Society of America, Abstracts* **11:**468.

Longhi J., Vander Auwera J., Fram M. S., Duchesne J.-C. (1999) Some phase equilibrium constraints on the origin of Proterozoic (massif) anorthosites and related rocks. *Journal of Petrology* **40:**339–362.

Martel C., Pichavant M., Holtz F., Scaillet B., Bourdier J.-L., Traineau H. (1999) Effects of $fO_2$ and $H_2O$ on andesite phase relations between 2 and 4 kbar. *Journal of Geophysical Research* **104:**29453–29479.

Möller C. (1998) Decompressed eclogites in the Sveconorwegian (-Grenvillian) orogen of SW Sweden: petrology and tectonic implications. *Journal of Metamorphic Geology* **16:**641–656.

Morimoto N., Fabries J., Ferguson A. K., Ginzburg I. V., Ross M., Seifert F. A., Zussman J., Aoki K., Gottardi G. (1988) Nomenclature of pyroxenes. *American Mineralogist* **73:**1123–1133.

Naney M. T. (1983) Phase equilibria of rock-forming ferromagnesian silicates in granitic systems. *American Journal of Science* **283:**993–1033.

Nogarède P. (2001) Etude minéralogique et géochimique de la pegmatite d'Eitland, complexe de Lyngdal, Norvège méridionale. Unpublished licenciate memoir. University of Liège56.

Pallister J. S., Hoblitt R. P., Meeker G. P., Newhall C. G., Knight R. J., Siems D. F. (1996) Magma mixing at Mount Pinatubo volcano: petrographical and chemical evidence from the 1991 deposits. In Newhall C. G. and Punongbayan R. S. (Eds.). Fire and Mud. Eruptions and Lahars of Mount Pinatubo, Philippines(Philippine Institute of Volcanology and Seismology, Quezon City) pp. 687–732 Seattle: University of Washington Press.

Pasteels P., Demaiffe D., Michot J. (1979) U–Pb and Rb–Sr geochronology of the eastern part of the South Rogaland igneous complex, southern Norway. *Lithos* **12:**199–208.

Prouteau G. (1999) Contribution des produits de fusion de la croûte océanique subductée au magmatisme d'arc: exemples du Sud-Est asiatique et approche expérimentale. Ph.D. thesis,Université de Bretagne occidentale.

Prouteau G. and Scaillet B. (2003) Experimental constraints on the origin of the 1991 Pinatubo dacite. *Journal of Petrology* **44:**2203–2241.

Rapp R. P. and Watson E. B. (1995) Dehydration melting of metabasalt at 8–32 kbar: implications for continental growth and crust–mantle recycling. *Journal of Petrology* **36:**891–931.

Robie R. A., Hemingway B. S., Fisher J. R. (1979) Thermodynamic properties of minerals and related substances at 298.15 K and 1 bar ($10^5$ Pa) pressure and at higher temperatures. *US Geological Survey Bulletin* **1452:**456.

Roux J. and Lefèvre A. (1992) A fast-quench device for internally heated pressure vessels. *European Journal of Mineralogy* **4:**279–281.

Rutherford M. J. and Devine J. D. (1996) Pre-eruption pressure–temperature conditions and volatiles in the 1991 Mount Pinatubo magma. *Fire and Mud: Eruptions and Lahars of Mount Pinatubo* (Philippine Institute of Volcanology and SeismologyIn Newhall C. G. and Punongbayan R. S. (Eds.). , Quezon City)751–766 Seattle, WA: University of Washington Press.

Scaillet B. and Evans B. W. (1999) The June 15, 1991 eruption of Mount Pinatubo. Phase equilibria and preeruption $P$–$T$–$f\mathrm{O}_2$–$f\mathrm{H}_2\mathrm{O}$ conditions of the dacite magma. *Journal of Petrology* **40:**381–411.

Scaillet B., Pichavant M., Roux J., Humbert G., Lefèvre A. (1992) Improvements of the Shaw membrane technique for measurement and control of $f\mathrm{H}_2$ at high temperatures and pressures. *American Mineralogist* **77:**647–655.

Scaillet B., Pichavant M., Roux J. (1995) Experimental crystallization of leucogranite magmas. *Journal of Petrology* **36:**663–705.

Scaillet B., Holtz F., Pichavant M. (1998) Phase equilibrium constraints on the viscosity of silicic magmas—1. Volcanic–plutonic association. *Journal of Geophysical Research* **103:**27257–27266

Schärer U., Wilmart E., Duchesne J.-C. (1996) The short duration and anorogenic character of anorthosite magmatism: U–Pb dating of the Rogaland complex, Norway. *Earth and Planetary Science Letters* **139:**335–350.

Sisson T. W. and Grove T. L. (1993) Experimental investigation of the role of $H_2O$ in calc-alkaline differentiation and subduction zone magmatism. *Contributions to Mineralogy and Petrology* **113:**143–166.

Smith D. R., Noblett J., Wobus R. A., Unruh D., Douglass J., Beane R., Davis C., Goldman S., Kay G., Gustavson B., Saltoun B., Stewart J. (1999) Petrology and geochemistry of late-stage intrusions of the A-type, mid-Proterozoic Pikes Peak batholith (Central Colorado, USA): implications for petrogenetic models. *Precambrian Research* **98:**271–305.

Stormer J. C. (1983) The effects of recalculation on estimates of temperature and oxygen fugacity from analyses of multicomponent iron–titanium oxides. *American Mineralogist* **68:**586–594.

Svedrup T. L. (1960) The pegmatite dyke at Rømteland. *Norges Geologiske Undersøkelse* **211:**124–196.

Vander Auwera J. and Longhi J. (1994) Experimental study of a jotunite (hypersthene monzodiorite): constraints on the parent magma composition and crystallization conditions ($P, T, f\mathrm{O}_2$) of the Bjerkreim–Sokndal layered intrusion (Norway). *Contributions to Mineralogy and Petrology* **118:**60–78.

Vander Auwera J., Longhi J., Duchesne J.-C. (1998) A liquid line of descent of the jotunite (hypersthene monzodiorite) suite. *Journal of Petrology* **39:**439–468.

Vander Auwera J., Liégeois J.-P., Demaiffe D., Bolle O., Bogaerts M., Duchesne J.-C. (2001) Two distinct post-collisional magmatic suites in the Sveconorwegian of southern Norway: consequence for the evolution of the Proterozoic continental lithosphere. *Journal of Conference Abstracts* **6:**769.

Vander Auwera J., Bogaerts M., Liégeois J.-P., Demaiffe D., Wilmart E., Bolle O., Duchesne J.-C. (2003) Derivation of the 1·0–0·9 Ga A-type granitoids of southern Norway by extreme differentiation from gabbros. *Precambrian Research* **124:**107–148.

Verhoogen J. (1962) Oxidation of iron–titanium oxides in igneous rocks. *Journal of Geology* **79:**168–181.

Vernon R. H. (1986) K-feldspar megacrysts in granites—phenocrysts or porphyroblasts. *Earth-Science Reviews* **23:**1–63.

Villiger S., Ulmer P., Müntener O., Thomson A. B. (2004) The liquid line of descent of anhydrous, mantle-derived, tholeiitic liquids by fractional and equilibrium crystallization—an experimental study at 1·0 GPa. *Journal of Petrology* **45:**2369–2388.

Wall V. J., Clemens J. D., Clarke D. B. (1987) Models of granitoid evolution and source composition. *Journal of Geology* **95:**731–749.

Wilmart E., Demaiffe D., Duchesne J.-C. (1989) Geochemical constraints on the genesis of the Tellnes ilmenite deposit, southwest Norway. *Economic Geology* **84:**1047–1056.

FIGURE

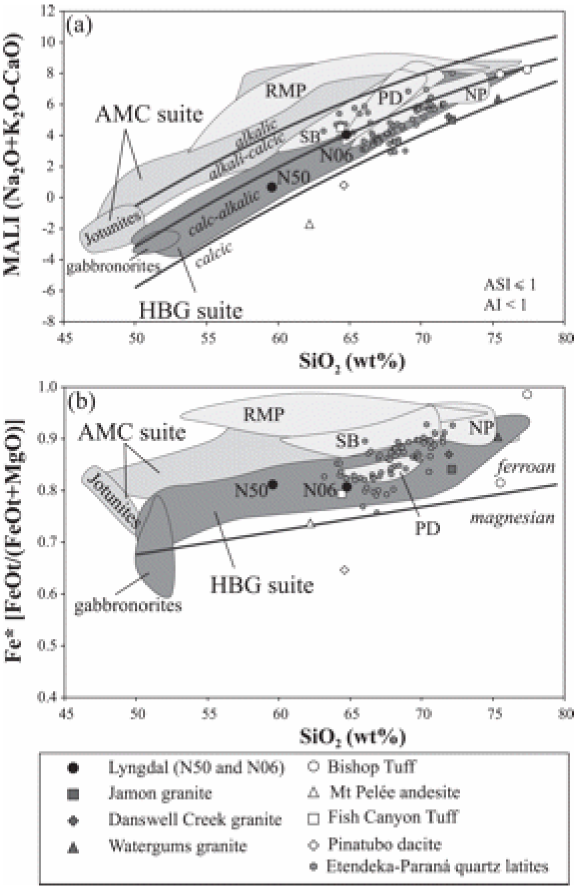

**Fig. 1** (a) MALI index plotted as a function of wt % $SiO_2$ and (b) Fe* as a function of wt % $SiO_2$ for Proterozoic granitoids associated with massif anorthosites or similar affinities: granitoids from the Rogaland anorthositic complex [AMC suite (Anorthosite–Mangerite–Charnockite): Wilmart *et al*. (1989), Duchesne & Wilmart (1997)] and associated hornblende–biotite plutons of the HBG suite (Hornblende–Biotite Granitoids), Nain Province (NP: Emslie & Stirling, 1993), Laramie anorthositic complex [RMP (Red Mountain Pluton): Anderson *et al*., 2003] and associated hornblende–biotite granitoids [SB (Sherman batholith): Frost *et al*., 1999], Parker Dam [PD: Anderson & Bender (1989); the other plutons from that study are not plotted for clarity]. Mafic rocks associated with the HBG suite (gabbronorites: Demaiffe *et al*., 1990; Bogaerts *et al*., 2003*a*) and of the AMC suite are also plotted (jotunites: Vander Auwera *et al*., 1998). Boundaries are from Frost *et al*. (2001). Data sources: Jamon granite from Dall'Agnol *et al*. (1999); Danswell Creek granite from Klimm *et al*. (2003); Watergums granite from Clemens *et al*. (1986); Bishop Tuff from Hildreth (1979), Etendeka–Paraná quartz latites from Garland *et al*. (1995) and Ewart *et al*. (1998); Fish Canyon Tuff from Johnson & Rutherford (1989*b*); Pinatubo dacite from Scaillet & Evans (1999); Mt. Pelée andesite from Martel *et al*. (1999).

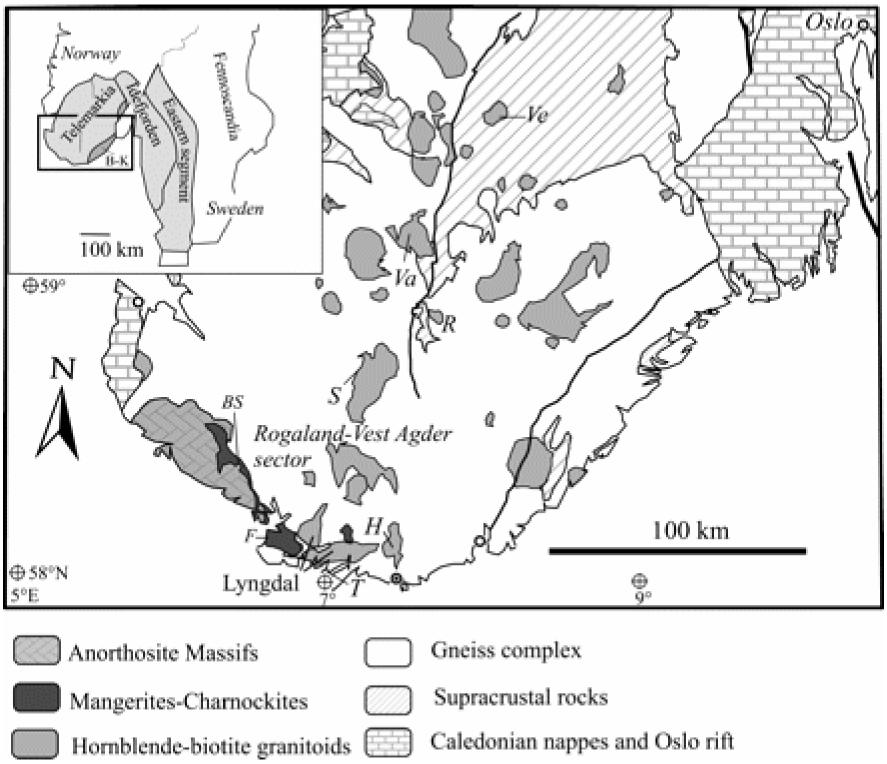

**Fig. 2** Simplified geological map of southern Norway [inset shows the area of the Sveconorwegian orogen (in grey); B-K, Bamble–Kongsberg sector], modified after Bingen *et al*. (2005). Abbreviations for HGB plutons: T, Tranevåg massif; H, Holum; S, Svöfjell; Va, Valle; R, Rustfjellet; Ve, Verhuskjerringi. Abbreviations for quartz mangerites–charnockites of the AMC suite: BS, Bjerkreim–Sokndal; F, Farsund.

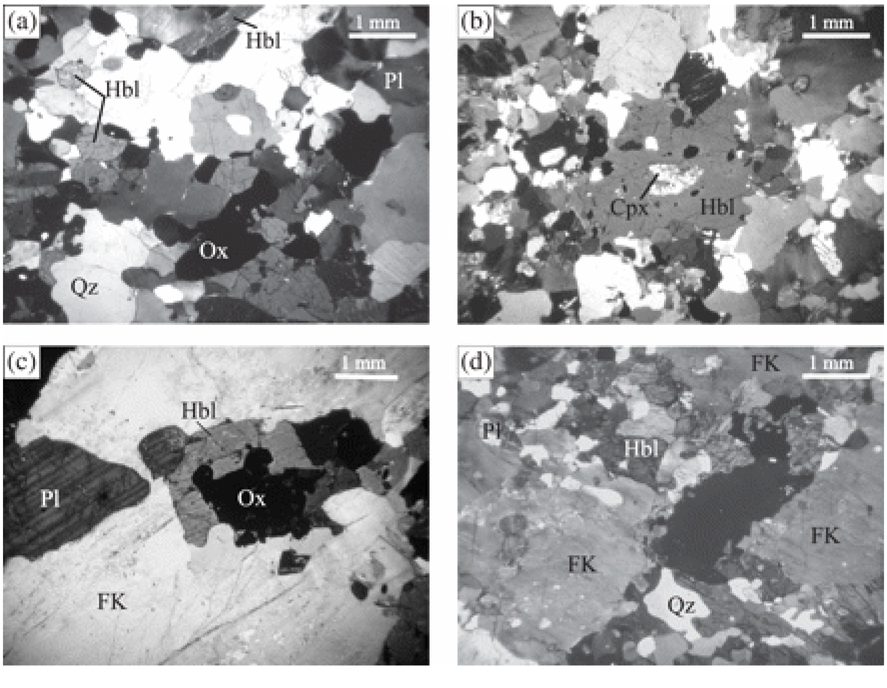

**Fig. 3** Photomicrographs (transmitted light with crossed Nicols) illustrating the mineralogy and structure in the Lyngdal granodiorite. (a) General structure of the rocks (note the euhedral shape of some amphiboles). (b) Relic of clinopyroxene in amphibole. (c) K-feldspar phenocryst (1 cm) with inclusions of amphibole, plagioclase and Fe–Ti oxides. (d) The three areas labelled FK denote a K-feldpar mineral in crystallographic continuity containing abundant inclusions of other minerals, suggesting its late crystallization. Cpx, clinopyroxene; FK, K-feldspar; Hbl, hornblende; Pl, plagioclase; Ox, Fe–Ti oxides; Qz, quartz.

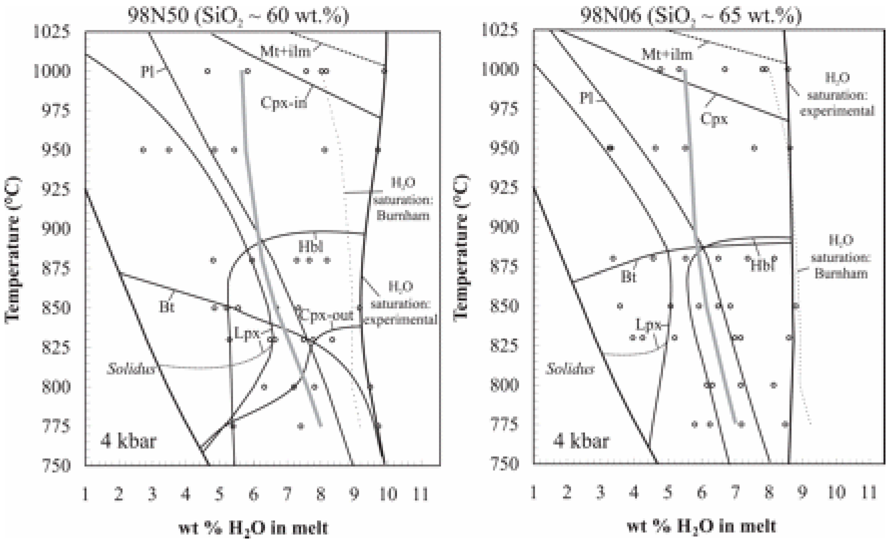

**Fig. 4** $T$–$H_2O^{melt}$ phase diagrams for the Lyngdal granodiorite (samples 98N50 and 98N06) at 4 kbar. $fO_2$ is between NNO – 0·4 and NNO + 0·8 except at 950 and 1000°C (see text). The fine dotted line is the $H_2O$ saturation curve calculated after Burnham (1979). The bold grey line is the $T$–$H_2O^{melt}$ path calculated for a closed system crystallizing with a bulk $H_2O$ content of 5 wt %. Inferred portions of mineral stability curves (Mt, Ilm, Lpx) are indicated by dashed lines. Mt, magnetite; Ilm, ilmenite; Hbl, amphibole; Cpx, clinopyroxene; Lpx, low-Ca pyroxene; Bt, biotite; Pl, plagioclase.

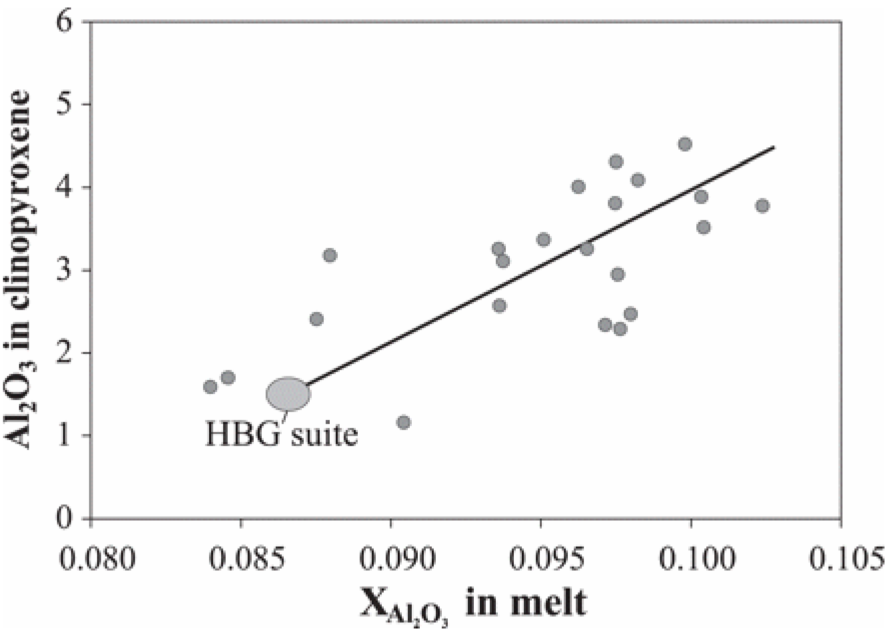

**Fig. 5** Evolution of the $Al_2O_3$ content (wt %) in the experimental clinopyroxenes plotted as a function of the molar fraction of $Al_2O_3$ ($X_{Al2O3}$) in the melts. The grey shaded area corresponds to the $Al_2O_3$ contents of the natural clinopyroxenes and the $X_{Al2O3}$ of the bulk-rocks of the HBG suite, which are assumed to represent melt compositions.

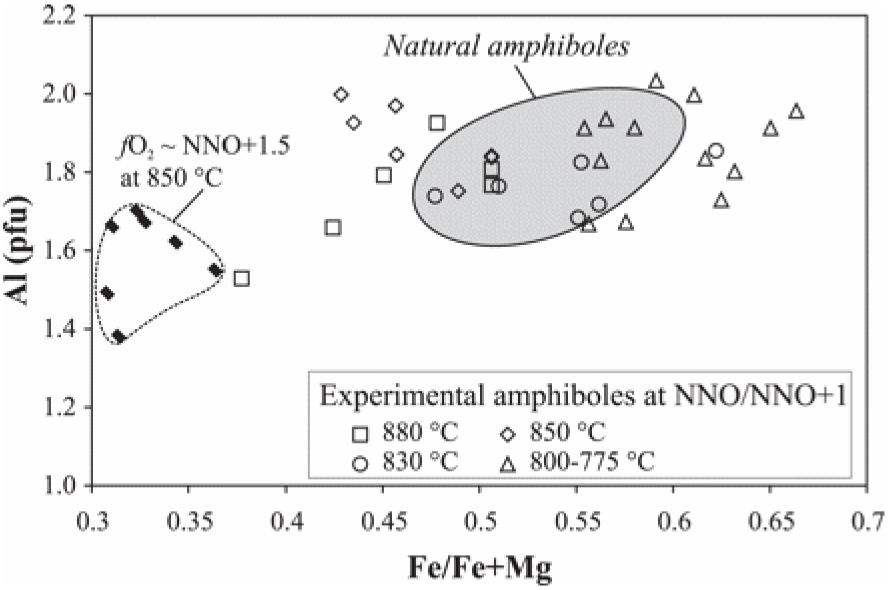

**Fig. 6** Amphibole compositions: Al (a.p.f.u.) plotted against Fe/(Fe + Mg) ratios, illustrating the compositional variation of the experimental amphiboles with $fO_2$ and pressure. Natural amphibole compositions are depicted by the shaded area.

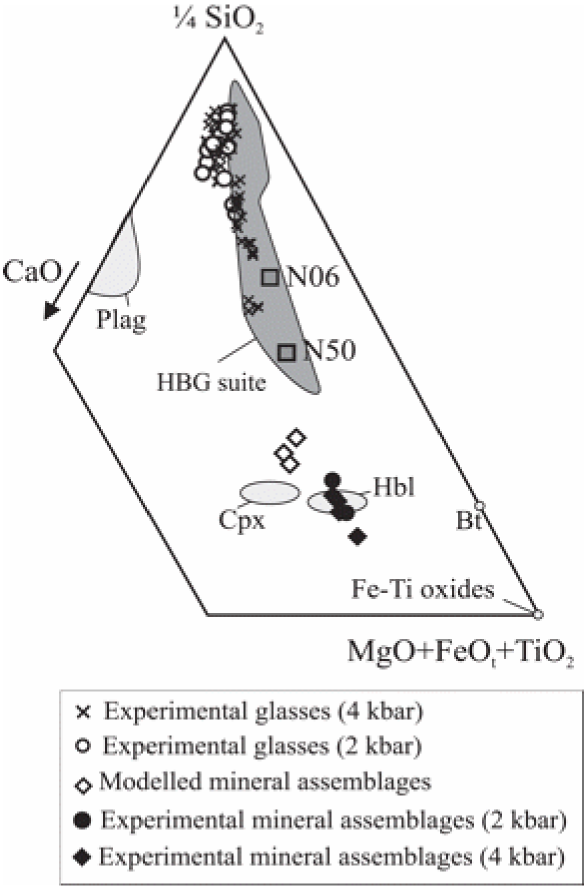

**Fig. 7** 1/4$SiO_2$–CaO–(MgO + $FeO_t$ + $TiO_2$) diagram (molar proportions) comparing experimental glasses with natural rocks from the HBG suite [data from Bogaerts *et al.* (2003*a*) and Vander Auwera *et al*. (2003); N06 and N50 correspond to the starting products]. The modelled mineral assemblages are obtained based on major element modelling by the least-squares method on natural rocks (Bogaerts *et al*., 2003*a*). The modal proportions of representative experimental mineral assemblages are given in Table 11. Plag, plagioclase; Cpx, clinopyroxene; Hbl, amphibole; Bt, biotite.

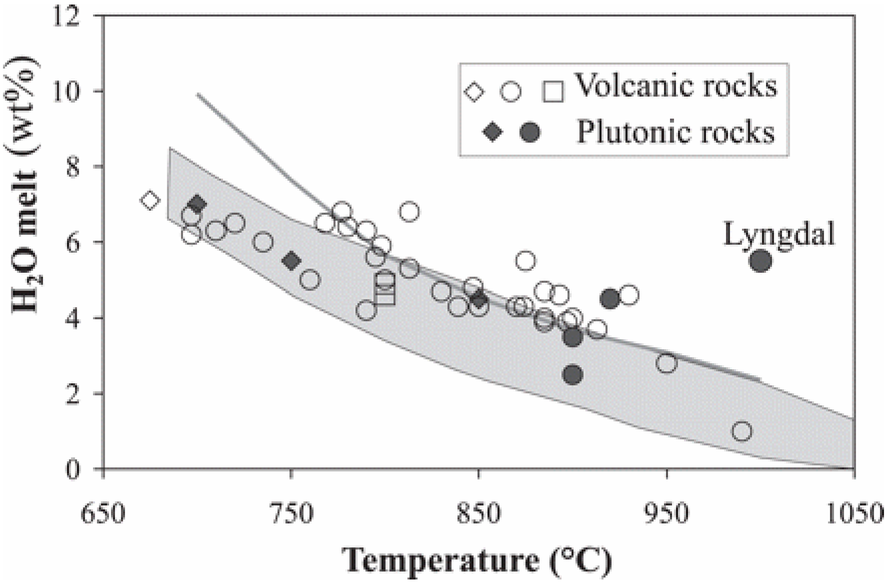

**Fig. 8** Relation between temperature (°C) and the $H_2O$ content (wt %) in melts of granitic composition determined from phase equilibrium experiments for plutonic and volcanic rocks or direct measurement of the $H_2O$ content in melt inclusions and Fe–Ti oxides for temperature (volcanic rocks). Original diagram from Scaillet *et al*. (1998), with added plutonic data from Klimm *et al*. (2003) and this study (Lyngdal). Circles, metaluminous or weakly peraluminous compositions; diamonds, peraluminous compositions; squares, peralkaline compositions. Modelled $T$–$H_2O^{melt}$ evolution during partial melting of a quartzofeldspathic rock (shaded area) between 3 and 10 kbar and an amphibolite (grey line) at 10 kbar. [See text for further details and Clemens & Watkins (2001) for the general procedure.]

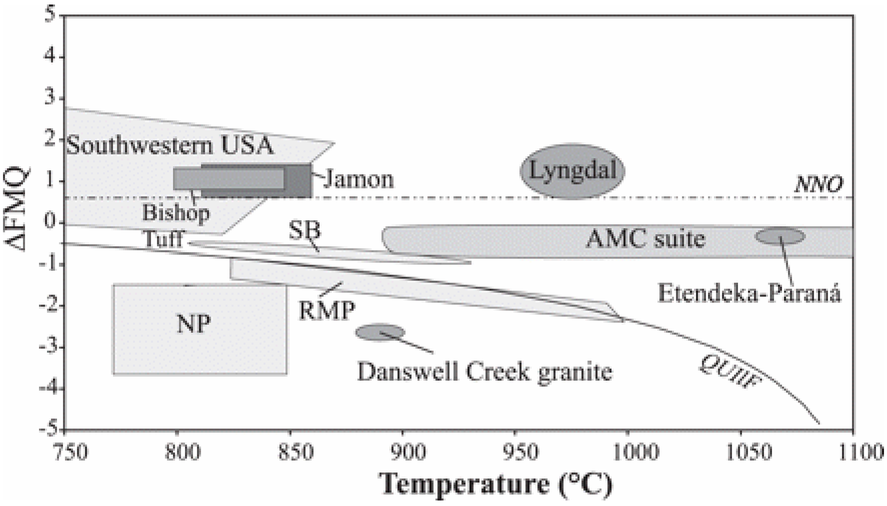

**Fig. 9** ΔFMQ [log $fO_2$(sample) – log $fO_2$(FMQ buffer)] vs temperature (°C), illustrating the diversity in $fO_2$ for metaluminous ferroan granitoids: Lyngdal (this study), AMC suite (Vander Auwera & Longhi, 1994; Duchesne & Wilmart, 1997), Jamon (Dall'Agnol *et al*.,

1999), Sherman batholith (SB: Frost *et al*., 1999), Red Mountain Pluton (RMP: Anderson *et al*., 2003), plutons from the Nain Province (NP: Emslie & Stirling, 1993), plutons from the Southwestern USA (Anderson & Bender, 1989), Danswell Creek granite (King *et al*., 2001; Klimm *et al*., 2003). $T$–$fO_2$ conditions estimated for the Bishop Tuff (Frost & Lindsley, 1992) and the Etendeka–Paraná quartz latites to rhyolites (Bellieni *et al*., 1986) are also plotted. The QUIlF curve refers to the Quartz–Ulvöspinel–Ilmenite–Fayalite equilibrium after Andersen *et al*. (1993).

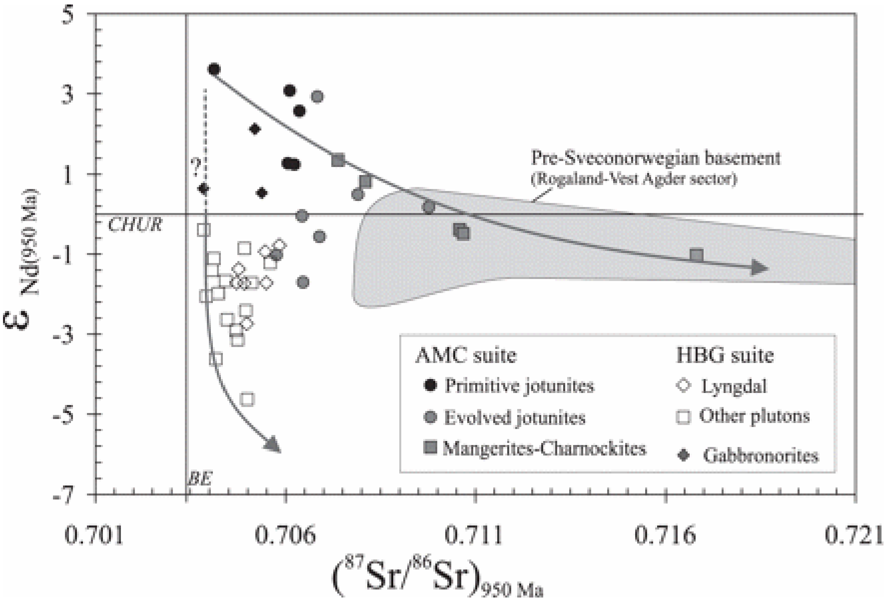

**Fig. 10** $\varepsilon_{\mathrm{Nd}(950\ \mathrm{Ma})}$ plotted as a function of the $(^{87}Sr/^{86}Sr)_{950\ Ma}$ for the HBG and AMC suites. The gabbronorites are also plotted. Data sources: Demaiffe *et al*. (1990); Bolle *et al*. (2003); Bogaerts *et al*. (2003*a*); Vander Auwera *et al*. (2003). The evolution from the jotunites to the charnockites (AMC suite) by crystallization and crustal contamination is well constrained (Duchesne & Wilmart, 1997; Vander Auwera *et al*., 1998); the link between the jotunites–grabbronorites and the HBG suite is hypothetical (see text). BE: $(^{87}Sr/^{86}Sr)_{950\ Ma}$ for the Bulk-Earth calculated from present ratios of $^{87}Sr/^{86}Sr = 0{\cdot}7047$ and $^{87}Rb/^{86}Sr = 0{\cdot}0850$; $\varepsilon_{\mathrm{Nd}}$ values are calculated relative to CHUR at 950 Ma with present ratios of $^{143}Nd/^{144}Nd = 0{\cdot}512638$ and $^{147}Sm/^{143}Nd = 0{\cdot}1967$ (Faure, 1986).

# TABLES

*Table 1 Composition of the starting materials (wt %) and comparison with other plutonic and volcanic rocks*

| | Lyngdal | | Lyngdal | | Lyngdal | Bjerkreim–Sokndal | Paraná quartz latite | Etendeka quartz latite | Fish Canyon Tuff | Pinatubo Tuff | Mt. Pelée andesite |
|---|---|---|---|---|---|---|---|---|---|---|---|
| | 98N50 | | 98N06 | | MB99N32 | | | | | | |
| | Rock | Glass (8) | Rock | Glass (8) | Rock | ST3 | FG-40 | SMG060 | | | |
| $SiO_2$ | 60·2 | 60·40 (50) | 65·2 | 65·97 (59) | 64·9 | 65·1 | 65·3 | 67·0 | 64·4 | 64·6 | 62·2 |
| $TiO_2$ | 1·74 | 1·83 (08) | 1·11 | 1·18 (06) | 1·26 | 1·08 | 1·4 | 1·08 | 0·6 | 0·53 | 0·5 |
| $Al_2O_3$ | 13·8 | 13·43 (22) | 14·4 | 14·18 (23) | 13·3 | 14·3 | 13·2 | 12·8 | 17·0 | 16·5 | 17·5 |
| $FeO_t$ | 9·26 | 9·20 (21) | 5·80 | 5·57 (17) | 7·10 | 7·01 | 7·17 | 7·9 | 4·26 | 4·37 | 6·39 |
| MnO | 0·16 | 0·15 (06) | 0·10 | 0·11 (05) | 0·15 | 0·17 | 0·14 | 0·12 | 0·11 | 0·1 | 0·14 |
| MgO | 2·15 | 2·13 (08) | 1·39 | 1·29 (05) | 1·32 | 0·90 | 1·33 | 1·13 | 1·11 | 2·39 | 2·28 |
| CaO | 5·35 | 5·50 (10) | 3·51 | 3·72 (11) | 4·20 | 2·48 | 3·29 | 3·38 | 3·62 | 5·23 | 6·35 |
| $Na_2O$ | 3·15 | 3·27 (14) | 3·28 | 3·26 (20) | 3·12 | 3·67 | 3·58 | 3·01 | 4·04 | 4·49 | 3·59 |
| $K_2O$ | 2·88 | 3·15 (06) | 4·32 | 4·31 (05) | 3·13 | 4·92 | 3·9 | 4·05 | 4·06 | 1·54 | 1·06 |
| $P_2O_5$ | 0·85 | 0·92 (11) | 0·39 | 0·43 (05) | 0·64 | 0·36 | 0·47 | 0·32 | — | — | — |

Glass starting materials for Lyngdal analysed by electron microprobe and recalculated to 100%. Numbers in parentheses following ‘Glass’ are the number of replicate measurements averaged to obtain the reported analyses. Numbers in parentheses following oxide concentrations are 1 S.D. in terms of the last two units cited. Rock analyses of Lyngdal from Bogaerts *et al*. (2003*a*). Other data sources: Bjerkreim–Sokndal quartz mangerite from Duchesne & Wilmart (1997); Paraná quartz latite from Bellieni *et al*. (1986); Etendeka quartz latite from Ewart *et al*. (1998); Fish Canyon Tuff from Johnson & Rutherford (1989*b*); Pinatubo dacite from Pallister *et al*. (1996); Mt. Pelée andesite from Martel *et al*. (1999).

*Table 2 Exzperimental conditions, nature and phase proportions (wt %), sample 98N50*

| Charge | $XH_2O^{in}$ | Results | $\Sigma r^2$ | $H_2O^{melt}$ (wt %) | $\Delta$ NNO |
|---|---|---|---|---|---|
| P = *4094 bar, fast quench device*, T = *950°C, run duration 71 h* | | | | | |
| 50-1 | 1·00 | Gl(84·5), Cpx(4·7), Mt(4·4), Ilm(3·0), Ap(1·6) | 0·31 | 9·7 | — |
| 50-2 | 0·90 | Gl(83·7), Cpx(5·2), Mt(4·8), Ilm(3·1), Ap(1·8) | 0·30 | 8·1 | — |
| 50-3 | 0·80 | Gl(79·5), Cpx(10·8), Mt(4·6), Ilm(3·2), Ap(1·1) | 0·78 | 5·4 | — |
| 50-4 | 0·72 | Gl(80·8), Cpx(8·7), Mt(5·0), Ilm(3·0), Ap(1·6) | 0·34 | 4·8 | — |
| 50-5 | 0·59 | Gl(67·5), Cpx(9·3), Mt(6·4), Ilm(1·6), Pl(11·7), Lpx (1·5), Ap(1·5) | 0·01 | 3·5 | — |
| 50-6 | 0·51 | Gl(62·2), Cpx(8·1), Mt(4·1), Ilm(3·7), Pl(16·5), Lpx(3·6), Ap(1·6) | 0·04 | 2·7 | — |
| P = *4040 bar*, $PH_2$ = *7·26 bar*, T = *850°C, run duration 218 h* | | | | | |
| 50-7 | 1·00 | Gl(72·0), Hbl(16·2), Cpx(2·17), Mt(6·4), Ilm(1·4), Ap(2·0) | 0·01 | 9·2 | 0·79 |
| 50-8 | 0·89 | Gl(74·2), Hbl(16·6), Cpx(tr), Mt(6·9), Ilm(1·1), Ap(2·1) | 0·05 | 7·3 | 0·69 |
| 50-9 | 0·79 | Gl(71·8), Hbl(12·5), Cpx(3·9), Mt(5·4), Ilm(1·4), Pl(2·8), Ap(1·8) | 0·05 | 6·7 | 0·59 |
| 50-10 | 0·71 | Gl(61·5), Hbl(12·1), Cpx(4·5), Mt(5·6), Ilm(1·5), Pl (12·5), Ap(1·8), Lpx(tr) | 0·02 | 5·5 | 0·50 |
| 50-11 | 0·59 | Gl(49·7), Cpx(3·1), Mt(4·7), Ilm(1·85), Pl(25·1), Bt(1·06), Lpx(11·25), Ap(1·8), Hbl(tr) | 0·09 | 5·2 | 0·34 |
| 50-12 | 0·50 | Gl(49·6), Cpx(2·8), Mt(4·4), Ilm(2·0), Pl(25·5), Bt(1·3), Lpx(12), Ap(1·8) | <0·01 | 4·8 | 0·19 |
| P = *3895 bar*, $PH_2$ = *14·16 bar*, T = *800°C, run duration 259 h* | | | | | |
| 50-13 | 1·00 | Gl(69·2), Hbl(23·3), Mt(3·4), Ilm(1·8), Ap(1·7) | — | 9·5 | 0·07 |
| 50-14 | 0·87 | Gl(60·1), Hbl(23·5), Bt(2·3), Pl(7·5), Mt(tr), Ilm(5·2), Ap(1·7) | 0·05 | 7·8 | –0·05 |
| 50-15 | 0·77 | Gl(54·7), Hbl(33·8), Cpx(Tr), Bt(0·5), Pl(12·5), Mt (tr), Ilm(2·6), Ap | 0·07 | 7·2 | –0·15 |
| 50-16 | 0·7 | Gl, (Hbl), Cpx, Bt, Pl, Mt, Bt, Ap, Ilm | — | 6·3 | –0·23 |
| P = *4041 bar*, $PH_2$ = *12·08 bar*, T = *880°C, run duration 214 h* | | | | | |
| 50-17 | 1·00 | Gl(73·2), Hbl(12·3), Cpx(3·6), Mt(7·7), Ilm(0·7), Ap(2) | 0·05 | 8·2 | 0·41 |
| 50-18 | 0·87 | Gl(74·8), Hbl(17·6), Cpx(tr), Mt(5·81), Ilm(0·9), Ap(2·4) | 0·28 | 7·7 | 0·29 |
| 50-19 | 0·76 | Gl(73·3), Hbl(16·6), Cpx(1·9), Mt(6·5), Ilm(0·7), Ap(2·0) | 0·1 | 7·3 | 0·17 |
| 50-20 | 0·65 | Gl(63·9), Hbl(13·9), Cpx(5·1), Mt(5·5) Ilm(1·0), | 0·08 | 6·0 | 0·03 |

| | | | | | |
|---|---|---|---|---|---|
| | | Pl(8·9), Ap(1·7), Lpx(tr) | | | |
| 50-21 | 0·58 | Leaked charge | | | |
| 50-22 | 0·50 | Gl(53·4), Mt(5·1), Ilm(1·6), Cpx(6·7), Pl(22·8), Lpx(8·5), Ap(1·7) | 0·04 | 4·8 | –0·19 |
| P = *3994 bar*, P$H_2$ *= 13·51 bar*, T = *830°C, run duration 309 h* | | | | | |
| 50-23 | 1·00 | Gl(71·6), Hbl(20·5), Mt(5·1), Ilm(1·4), Ap(1·8) | 0·14 | 8·3 | 0·20 |
| 50-24 | 0·84 | Gl(68·8), Hbl(23·6), Mt(3·8), Ilm(1·4), Ap(1·9), Cpx(tr) | 0·08 | 7·8 | 0·05 |
| 50-25 | 0·78 | Gl(61·8), Hbl(22·9),Mt(3·6), Ilm(1·6), Pl(8·73), Bt(0·2), Ap(1·7), Cpx(tr) | 0·03 | 7·5 | –0·01 |
| 50-26 | 0·7 | Gl(56·8), Hbl(21·0), Cpx(0·9), Mt(3·7), Ilm(1·7), Pl(13·6), Bt(0·4), Ap(1·7), Lpx(tr) | <0·01 | 6·6 | –0·11 |
| 50-27 | 0·57 | Gl(40·8), Cpx(13·8), Mt(2·8), Ilm(2·4), Lpx(2·1), Pl(30·3), Bt(4·9), Ap(1·8), Hbl(tr) | <0·01 | 6·5 | –0·28 |
| 50-28 | 0·49 | Gl(33·2), Cpx(tr), Lpx(18·23), Mt(0·8), Ilm(2·6), Pl(37·9), Bt(4·8), Ap(1·7) | 0·04 | 5·3 | –0·42 |
| P = *4142 bar*, P$H_2$ *= 8·60 bar*, T = *775°C, run duration 272 h* | | | | | |
| 50-29 | 1·00 | Gl(69·7), Hbl(23·9), Mt(3·6), Ilm(1·8), Ap | 0·63 | 7·3 | –0·031 |
| 50-30 | 0·93 | Gl(57·4), Hbl(27), Bt(tr), Pl(13·2), Mt(3·1), Ilm(1·5), Ap | 0·04 | 7·4 | –0·094 |
| 50-31 | 0·73 | Gl(51), Hbl(25·4), Bt(2·6), Pl(15·9), Mt(1·8), Ilm(2·3), Ap | 0·57 | 5·4 | –0·304 |
| P = *2050 bar, pressure vessel Basset*, T = *850°C, run duration 318 h* | | | | | |
| 50-33 | 1·00 | Gl(61·0), Hbl(3·4), Cpx(6·7), Mt(9·3), Ilm(2·0), Pl(15·0), Bt(2·2), Ap(1·1) | 0·025 | 5·7 | — |
| 50-34 | 0·89 | Gl(56·8), Hbl(2·9), Cpx(6·0), Mt(8·5), Ilm(2·3), Pl(20·6), Bt(1·7), Ap(1·3) | <0·01 | 5·9 | — |
| 50-35 | 0·80 | Gl(51·4), Hbl(2·7), Cpx(6·5), Mt(9·0), Ilm(2·0), Pl(25·4), Bt(2·1), Ap(1·8) | <0·01 | 5·7 | — |
| 50-36 | 0·71 | Gl(47·0), Cpx(8·0), Mt(9·1), Ilm(2·0), Pl(29·6), Bt(3·6), Ap(1,7) | 0·11 | 3·4 | — |
| Charge | $H_2O$(wt%) | Results | $\Sigma r^2$ | $H_2O^{melt}$ | Δ NNO |
| P = *3750 bar, fast quench device*, T = *1000°C, run duration 48 h* | | | | | |
| 50-39 | 14·9 | Gl(92·0), Mt(5·4), Ilm(2·6) | — | 9·9 | — |
| 50-40 | 8·52 | Gl, Mt, Ilm | — | 8·2 | — |
| 50-41 | 7·84 | Gl, Mt, Ilm | — | 8·0 | — |
| 50-42 | 6·70 | Gl, Mt, Ilm | — | 7·6 | — |
| 50-43 | 5·91 | Gl, Mt, Ilm, Cpx | — | 5·8 | — |

|  |  |  |  |  |  |
|---|---|---|---|---|---|
| 50-44 | 4·47 | Gl, Mt, Ilm, Cpx | — | 4·6 | — |
| P = *1912 bar, pressure vessel Gros Bleu*, $PH_2$ = *1·77*, T = *850°C, run duration 192 h* |  |  |  |  |  |
| 50-46 | 6·15 | Gl(66·7), Hbl(9·0), Cpx(2·8), Mt(8·0), Ilm(2·0), Pl(9·9), Ap(1·2) | 0·1 | 7·9 | 1·5 |
| 50-47 | 5·38 | Gl(70·0), Hbl(10·0), Cpx(2·1), Mt(7·0), Ilm(1·0), Pl(8·0), Ap(1·4) | 0·03 | 8·1 | — |
| 50-48 | 4·88 | Gl(66·2), Hbl(7·0), Cpx(3·9), Mt(6·9), Ilm(1·4), Pl(11·2), Bt(1·6), Ap(1·2) | <0·01 | 8·2 | — |
| 50-49 | 4·15 | Gl(63·5), Hbl(8·6), Cpx(1·9), Mt(5·0), Ilm(1·6), Pl(16·0), Bt(2·0), Ap(1·2) | 0·015 | 6·7 | — |
| 50-50 | 3·39 | Gl(63·0), Hbl(12·5), Mt(5·9), Ilm(1·3), Pl(16·5), Bt(tr), Ap(1·3) | 0·013 | 5·3 | — |

*Table 3 Experimental conditions, nature and phase proportions (wt %), sample 98N06*

| Charge | $XH_2O^{in}$ | Results | $\Sigma r^2$ | $H_2O^{melt}$ (wt %) | Δ NNO |
|---|---|---|---|---|---|
| P = *4094 bar*, T = *950°C, run duration 71 h* | | | | | |
| 06-2 | 0·91 | Gl(92·7), Cpx(1·5), Mt(2·3), Ilm(1·3), Ap(0·7) | 0·25 | 7·5 | — |
| 06-3 | 0·78 | Gl(91·3), Cpx(2·3), Mt(2·4), Ilm(1·6), Ap(0·6) | 0·34 | 5·5 | — |
| 06-4 | 0·7 | Gl(90·6), Cpx(3·8), Mt(2·6), Ilm(1·2), Ap(0·5) | 0·19 | 4·6 | — |
| 06-5 | 0·59 | Gl(83·3), Cpx(4·5), Mt(2·5), Ilm(1·8), Pl(6·11), Ap(0,3) | 0·07 | 3·2 | — |
| 06-6 | 0·48 | Gl(90·5), Cpx(4·0), Mt(2·7), Ilm(1·2), Ap(0·3) | 0·21 | 3·3 | — |
| P = *4040 bar*, $PH_2$ = *7·26 bar*, T = *850°C, run duration 218 h* | | | | | |
| 06-7 | 1 | Gl(84·8), Cpx(tr), Hbl(5·1), Mt(2·5), Ilm(0·6), Bt(0·6), Ap(1·2) | 0·17 | 8·8 | 0·79 |
| 06-8 | 0·87 | Gl(82·8), Cpx(3·0), Hbl(1·8), Mt(3·2), Ilm(0·6), Bt(7·5), Ap(0·8) | 0·11 | 6·8 | 0·67 |
| 06-9 | 0·78 | Gl, Cpx, Hbl, Mt, Ilm, Bt, Ap | — | 6·5 | 0·58 |
| 06-10 | 0·71 | Gl(77·8), Cpx(4·6), Mt(2·7), Ilm(0·6), Bt(7·0), Pl(6·1), Ap(0·8), Hbl(tr) | 0·01 | 5·9 | 0·50 |
| 06-11 | 0·6 | Gl(66·3), Cpx(5·9), Mt(2·4), Ilm(0·8), Bt(8·8), Pl(16·1), Ap(0·8), Lpx(tr) | 0·03 | 5·0 | 0·35 |
| 06-12 | 0·48 | Gl(64·9), Cpx(4·0), Mt(2·0), Ilm(1·1), Bt(6·1), Pl(18·3), Ap(0·8), Lpx(2·2) | <0·01 | 3·6 | 0·16 |
| P = *3895 bar*, $PH_2$ = *14·16 bar*, T = *800°C, run duration 259 h* | | | | | |
| 06-13 | 1 | Gl(81·1), Cpx(0·2), Hbl(5·9), Mt(1·6), Ilm(0·6), Bt(9·7), Ap(0·4) | 0·13 | 8·1 | 0·07 |
| 06-14 | 0·87 | Gl, Cpx, Hbl, Mt, Ilm, Bt, Pl, Ap | — | 7·2 | –0·05 |
| 06-15 | 0·79 | Gl(75·7), Cpx(2·7), Hbl(5·9), Mt(tr), Ilm(1·2), Bt(10·1), Pl(5·9), Ap(0·8) | <0·01 | 6·3 | –0·15 |
| 06-16 | 0·68 | Gl(58·9), Cpx(5·76), Mt(0·2), Ilm(0·8), Bt(14·6), Pl(18·6), Ap(0·9) | <0·01 | 6·1 | –0·23 |
| P = *4041 bar*, $PH_2$ = *12·08 bar*, T = *880°C, run duration 214 h* | | | | | |
| 06-17 | 1·00 | Gl(84·0), Cpx(2·2), Hbl(1·3), Mt(4·0), Ilm(tr), Bt(6·8), Ap(1·0) | 0·02 | 8·2 | 0·41 |
| 06-18 | 0·86 | Gl(83), Cpx(3·2), Hbl(2·3), Mt(3·9), Ilm(tr), Bt(6·1), Ap(1·0) | 0·10 | 7·4 | 0·28 |
| 06-19 | 0·76 | Gl(82·0), Cpx(4·9), Hbl(2·6), Mt(2·6), Ilm(0·3), Bt(5·5), Ap(0·8) | 0·03 | 6·5 | 0·17 |
| 06-20 | 0·63 | Gl(80·5), Cpx(6·0), Mt(3·7), Ilm(0·2), Bt(5·8), Pl(3·6), Ap(0·8) | 0·03 | 5·5 | 0·01 |

| | | | | | |
|---|---|---|---|---|---|
| 06-21 | 0·56 | Gl(72·5), Cpx(5·9), Mt(1·8), Ilm(0·5), Bt(5·4), Pl(11·6), Lpx(1·7), Ap(0·6) | <0·01 | 4·6 | –0·09 |
| 06-22 | 0·50 | Gl, Cpx, Mt, Ilm, Pl, Lpx, Ap | — | 3·4 | –0·19 |
| P = *3994 bar*, P$H_2$ = *13·51 bar*, T = *830°C, run duration 309 h* | | | | | |
| 06-23 | 1·00 | Gl(82·3), Cpx(2·9), Hbl(0·6), Mt(3·5), Ilm(0·3), Bt(8·6), Ap(1·0) | 0·13 | 8·6 | 0·20 |
| 06-24 | 0·88 | Gl(82·6), Cpx(2·1), Hbl(3·7), Mt(2·9), Ilm(0·5), Bt(6·9), Ap(0·9) | 0·06 | 7·2 | 0·09 |
| 06-25 | 0·80 | Gl(81·8), Cpx(0·7), Hbl(6·4), Mt(2·0), Ilm(0·5), Bt(7·2), Ap(0·9) | 0·14 | 7·0 | 0·01 |
| 06-26 | 0·69 | Gl(70·4), Cpx(4·9), Mt(3·6), Ilm(0·4), Bt(7·8), Pl(12·5), Ap(0·8) | <0·01 | 5·2 | –0·12 |
| 06-27 | 0·58 | Gl(61·2), Cpx(3·9), Mt(2·3), Ilm(0·9), Bt (8·7), Pl(20·2), Lpx(1·6), Ap(0·8) | 0·01 | 4·2 | –0·27 |
| 06-28 | 0·50 | Gl(59·5), Cpx(2·6), Mt(1·7), Ilm(1·1), Bt(8·0), Lpx(3·8), Pl(22·0), Ap(0·8) | <0·01 | 4·0 | –0·40 |
| P = *4142 bar*, P$H_2$ = *8·60 bar*, T = *775°C, run duration 272 h* | | | | | |
| 06-29 | 1·00 | Gl, Cpx, Hbl, Bt, Mt, Ilm, Ap | — | 7·3 | –0·03 |
| 06-30 | 0·89 | Gl(68·1), Cpx (2·3), Hbl (8·2), Bt(7·9), Pl(10·8), Mt (1·1), Ilm(1·1), Ap | 0·02 | 7·1 | –0·13 |
| 06-31 | 0·78 | Gl(61·8), Cpx(7·1), Bt(12·5), Pl(15·8), Mt(1·1), Ilm(1·1), Ap | <0·01 | 6·2 | –0·25 |
| 06-32 | 0·66 | Gl(58·8), Cpx(0·7), Bt(12·4), Pl(19), Mt(1·0), Ilm(1·2), Ap | 0·02 | 5·8 | –0·39 |
| P = *2050 bar, pressure vessel Basset*, T = *850°C, run duration 318 h* | | | | | |
| 06-33 | 1 | Gl, Mt, Ilm, Bt, Pl, Ap | — | 6·5 | — |
| 06-34 | 0·88 | Gl(70·6), Mt(5·3), Ilm(1·1), Bt(9·2), Pl(12·7), Ap(1·1) | 0·74 | 5·9 | — |
| 06-35 | 0·81 | Gl(69·1), Mt(5·2), Ilm(1·1), Bt(5·9), Pl(18·1), Ap(0·9) | 0·63 | 4·8 | — |
| 06-36 | 0·72 | Gl(64·3), Mt(5·0), Ilm(1·2), Bt(6·9), Pl(21·7), Ap(3·1) | 1·83 | 4·3 | — |
| Charge | $H_2O$(wt%) | Results | $\Sigma r^2$ | $H_2O^{melt}$ | $\Delta$ NNO |
| P = *3750 bar, fast quench device*, T = *1000°C, run duration 48 h* | | | | | |
| 06-39 | 14·4 | Gl(96), Mt(3·5), Ilm(0·5) | — | 8·6 | — |
| 06-40 | 9·00 | Gl(96), Mt(3·9), Ilm(0·1) | — | 7·8 | — |
| 06-41 | 8·18 | Gl(96), Mt(3·7), Ilm(0·3) | — | 7·9 | — |
| 06-42 | 7·44 | Gl(96), Mt(3·5), Ilm(0·5) | — | 6·7 | — |
| 06-43 | 5·72 | Gl(95), Mt(4·0), Ilm(1·0) | — | 4·8 | — |

|  |  |  |  |  |  |
|---|---|---|---|---|---|
| 06-44 | 3·93 | Gl(96), Mt(2·6), Ilm(1·4) | — | 5·3 | — |
| P = *1912 bar, pressure vessel Gros Bleu*, P$H_2$ = *1·77*, T = *850°C, run duration 192 h* |  |  |  |  |  |
| 06-45 | 10·43 | Gl(84·0), Mt(4·0), Ilm(0·7), Bt (8·7), Ap(1·6) | 0·5 | 7·6 | 1·5 |
| 06-47 | 5·28 | Gl(80·0), Cpx(2·7), Mt(4·4), Ilm(tr), Bt (6·0), Pl(5·0), Ap(0·8) | 0·31 | 5·9 | — |
| 06-48 | 4·78 | Gl(74·7), Cpx(2·6), Mt(3·7), Ilm(0·8), Bt (6·0), Pl(10·9), Ap(0·8) | 0·05 | 6·1 | — |
| 06-49 | 4·18 | Gl(69·2), Cpx(2·6), Mt(2·2), Ilm(0·6), Bt (8·1), Pl(15·9), Ap(0·3) | 0·015 | 6·8 | — |
| 06-50 | 3·25 | Gl(66·8), Cpx(1·8), Mt(3·7), Ilm(0·6), Bt (7·8), Pl(18·2), Ap(1·0) | 0·09 | 4·1 | — |

$\Delta$NNO = log $fO_2$(experiment) – log $fO_2$(NNO) (Chou, 1987). $XH_2O^{in}$, molar ratio $H_2O/(H_2O + CO_2)$ loaded in the capsule. Gl, glass; Pl, plagioclase; Hbl, hornblende; Cpx, clinopyroxene; Bt, biotite, Mt, magnetite; Ilm, ilmenite; Ap, apatite; Lpx, low-calcium pyroxene (orthopyroxene or pigeonite).

*Table 4 Representative compositions of ilmenite and magnetite*

| | Experimental | | | | | | | | Natural | |
|---|---|---|---|---|---|---|---|---|---|---|
| | 950°C | 950°C | 880°C | 1000°C | 950°C | 880°C | 850°C | 775°C | Bishop Tuff | |
| | 50-1 | 50-2 | 06-17 | 50-39 | 50-1 (2) | 06-17 (2) | 06-7 (7) | 06-29 (5) | Early | Late |
| $TiO_2$ | 25·16 | 26·11 | 45·75 | 2·35 | 5·01 (16) | 11·62 (21) | 9·07 (19) | 7·13 (25) | 8·95 | 9·45 |
| $Al_2O_3$ | 0·55 | 0·67 | 0·17 | 2·08 | 2·07 (06) | 1·97 (01) | 1·99 (11) | 1·80 (08) | 0·85 | 1·35 |
| $Fe_2O_3$ | 51·80 | 53·71 | 5·65 | 58·29 | 55·52 | 42·53 | 49·10 | 54·02 | 49·49 | 47·75 |
| FeO | 18·58 | 12·12 | 46·10 | 34·45 | 32·35 | 41·27 | 36·15 | 34·27 | 40·41 | 40·34 |
| MgO | 2·11 | 1·94 | 2·06 | 3·56 | 2·95 (10) | 1·28 (08) | 1·14 (04) | 0·42 (04) | 0·25 | 0·75 |
| MnO | 0·28 | 0·20 | 0·38 | 0·27 | 0·54 (13) | 0·29 (20) | 0·42 (15) | 0·32 (08) | 0·90 | 0·43 |
| Total | 98·48 | 94·75 | 100·10 | 100·98 | 98·43 | 98·95 | 97·86 | 97·95 | 100·86 | 100·08 |
| Ti | 0·489 | 0·507 | 0·888 | 0·067 | 0·143 | 0·333 | 0·260 | 0·204 | 0·256 | 0·270 |
| Al | 0·017 | 0·020 | 0·005 | 0·093 | 0·093 | 0·088 | 0·089 | 0·081 | 0·038 | 0·061 |
| $Fe^{3+}$ | 1·006 | 1·072 | 0·107 | 1·630 | 1·579 | 1·210 | 1·410 | 1·559 | 1·407 | 1·358 |
| $Fe^{2+}$ | 0·401 | 0·269 | 0·968 | 1·071 | 1·022 | 1·305 | 1·154 | 1·099 | 1·277 | 1·275 |
| Mg | 0·081 | 0·075 | 0·079 | 0·202 | 0·167 | 0·072 | 0·064 | 0·024 | 0·014 | 0·043 |
| Mn | 0·006 | 0·004 | 0·008 | 0·009 | 0·017 | 0·009 | 0·013 | 0·010 | 0·029 | 0·014 |
| $X_{\mathrm{Ilm}}$ | 47 | 41 | 95 | — | — | — | — | — | — | — |
| $X_{\mathrm{Usp}}$ | — | — | — | 7 | 14 | 36 | 27 | 21 | 27 | 29 |

% ilmenite in hemoilmenite ($X_{\mathrm{Ilm}}$) and % ulvöspinel in titanomagnetite ($X_{\mathrm{Usp}}$) calculated after Stormer (1983). Bishop Tuff data from Hildreth (1979). Numbers in parentheses following charge names are the number of replicate measurements averaged to obtain the reported analyses. Numbers in parentheses following oxide concentrations are 1 S.D. in terms of the last two units cited.

*Table 5 Representative compositions of natural and experimental plagioclase*

| | Lyngdal | | | | | | | | Bishop Tuff | |
|---|---|---|---|---|---|---|---|---|---|---|
| | Natural | | | | Experimental | | | | | |
| | | | | | 880°C | 830°C | 800°C | 775°C | | |
| | 98N50 | 98N50 | 98N06 | 98N06 | 06-20 | 06-26 | 50-16 | 06-31 | Early | Late |
| $SiO_2$ | 61·49 | 61·46 | 62·80 | 61·74 | 56·17 | 60·65 | 62·56 | 61·41 | 64·50 | 62·50 |
| $Al_2O_3$ | 24·22 | 23·91 | 23·85 | 23·85 | 26·98 | 24·42 | 20·34 | 23·00 | 21·90 | 22·90 |
| FeO | 0·04 | 0·04 | 0·00 | 0·07 | 0·61 | 0·31 | 1·44 | 0·76 | 0·12 | 0·23 |
| CaO | 5·74 | 5·62 | 5·14 | 5·61 | 9·53 | 6·86 | 5·60 | 5·78 | 3·00 | 4·70 |
| $Na_2O$ | 8·26 | 8·62 | 8·68 | 8·40 | 5·62 | 6·25 | 6·93 | 6·87 | 9·40 | 8·20 |
| $K_2O$ | 0·24 | 0·33 | 0·21 | 0·32 | 0·59 | 1·12 | 1·43 | 1·34 | 1·10 | 1·35 |
| Total | 100·00 | 99·98 | 100·68 | 100·00 | 99·50 | 99·60 | 98·31 | 99·16 | 100·02 | 99·88 |
| An | 27 | 26 | 24 | 26 | 47 | 35 | 28 | 29 | 14 | 22 |
| Ab | 71 | 72 | 74 | 72 | 50 | 58 | 63 | 63 | 80 | 70 |
| Or | 1 | 2 | 1 | 2 | 3 | 7 | 9 | 8 | 6 | 8 |

Bishop Tuff data from Hildreth (1979).

*Table 6 Representative compositions of natural and experimental amphibole*

| | Lyngdal | | | | | | | | | |
|---|---|---|---|---|---|---|---|---|---|---|
| | Natural | | | Experimental | | | | | | |
| | 98N50 | 98N5 | 98N06 | 850°C | | 830°C | | 850°C | | 830°C |
| | | | | 50-9 (4) | 50-10 (3) | 50-25 (3) | 50-26 (2) | 06-10 | 06-9 (3) | 06-25 |
| $SiO_2$ | 43·12 | 43·95 | 42·50 | 41·82 (13) | 43·73 (99) | 43·16 (1·18) | 42·32 (1·11) | 40·99 | 42·61 (37) | 42·01 |
| $TiO_2$ | 1·84 | 1·92 | 1·59 | 2·14 (26) | 1·98 (06) | 2·07 (13) | 1·99 (03) | 2·34 | 2·06 (07) | 1·82 |
| $Al_2O_3$ | 10·05 | 9·16 | 9·56 | 10·98 (08) | 10·40 (23) | 9·28 (35) | 9·40 (19) | 10·03 | 10·22 (28) | 9·96 |
| FeO | 17·53 | 17·63 | 19·49 | 16·58 (64) | 16·85 (14) | 19·41 (31) | 20·83 (05) | 18·44 | 16·74 (16) | 19·48 |
| MnO | 0·49 | 0·50 | 0·45 | 0·28 (06) | 0·34 (13) | 0·35 (12) | 0·26 (07) | 0·25 | 0·30 (17) | 0·22 |
| MgO | 10·57 | 10·12 | 8·73 | 11·07 (18) | 11·23 (40) | 8·87 (33) | 9·12 (02) | 10·01 | 10·64 (18) | 8·85 |
| CaO | 11·34 | 11·89 | 11·81 | 11·08 (22) | 9·89 (35) | 10·93 (58) | 10·07 (21) | 10·68 | 11·11 (07) | 10·77 |
| $Na_2O$ | 1·69 | 1·76 | 1·81 | 1·91 (04) | 1·91 (09) | 1·64 (08) | 1·66 (04) | 1·71 | 1·73 (11) | 1·85 |
| $K_2O$ | 1·39 | 1·46 | 1·61 | 0·81 (07) | 0·76 (06) | 0·82 (11) | 0·75 (01) | 1·08 | 1·04 (10) | 0·90 |
| F | 0·94 | 0·71 | 1·08 | 0·24 (21) | 0·31 (22) | 0·11 (02) | 0·13 (12) | 0·78 | 0·58 (08) | 0·30 |
| Cl | 0·16 | 0·13 | 0·19 | 0·00 | 0·02 (03) | 0·02 (02) | 0·03 (04) | 0·00 | 0·02 (01) | 0·10 |
| Total | 99·12 | 99·23 | 98·82 | 97·47 | 97·49 | 96·67 | 96·54 | 96·30 | 97·05 | 96·26 |
| O = F, Cl | 0·43 | 0·33 | 0·50 | 0·10 | 0·13 | 0·05 | 0·06 | 0·33 | 0·25 | 0·15 |
| Total | 98·69 | 98·90 | 98·32 | 97·37 | 97·36 | 96·62 | 96·48 | 95·97 | 96·80 | 96·11 |
| $H_2O^*$ | 1·50 | 1·62 | 1·39 | 1·77 | 1·75 | 1·89 | 1·87 | 1·55 | 1·69 | 1·76 |
| Total | 100·19 | 100·52 | 99·71 | 99·14 | 99·11 | 98·51 | 98·34 | 97·52 | 98·48 | 97·88 |
| $X_{Fe}$ | 0·48 | 0·48 | 0·56 | 0·46 | 0·46 | 0·55 | 0·56 | 0·51 | 0·51 | 0·55 |

[*] Water calculated to fill up the (OH, F, Cl) group.

$X_{Fe}$ is Fe/ (Fe + Mg) cationic ratio. Numbers in parentheses following charge names are the number of replicate measurements averaged to obtain the reported analyses. Numbers in parentheses following oxide concentrations are 1 S.D. in terms of the last two units cited.

*Table 7 Representative compositions of natural and experimental biotite*

| | Lyngdal | | | | | | | | Bishop Tuff | |
|---|---|---|---|---|---|---|---|---|---|---|
| | Natural | | | Experimental | | | | | | |
| | 98N06 | 98N06 | 98N06 | 880°C | | 850°C | 830°C | 800°C | | |
| | | | | 06-18 (2) | 06-21 (3) | 06-9 (2) | 06-25 (3) | 06-14 (2) | Early | Late |
| $SiO_2$ | 37·70 | 37·69 | 37·11 | 36·35 (11) | 38·26 (1·55) | 37·09 (1·03) | 37·23 | 36·25 (1·21) | 35·60 | 36·70 |
| $TiO_2$ | 3·13 | 3·15 | 3·72 | 4·23 (01) | 5·32 (17) | 4·43 (0·25) | 4·42 | 4·16 (67) | 4·40 | 5·40 |
| $Al_2O_3$ | 12·94 | 12·73 | 12·90 | 14·20 (16) | 14·13 (24) | 14·76 (07) | 14·71 | 14·40 (06) | 12·50 | 13·00 |
| FeO | 19·17 | 19·07 | 20·43 | 17·58 (03) | 19·55 (56) | 18·28 (35) | 20·39 | 23·03 (40) | 25·10 | 18·90 |
| MnO | 0·33 | 0·26 | 0·26 | 0·26 (05) | 0·03 (05) | 0·09 (08) | 0·08 | 0·14 (05) | 0·40 | 0·15 |
| MgO | 12·26 | 12·20 | 10·82 | 12·61 (19) | 9·11 (39) | 11·63 (51) | 8·88 | 7·81 (07) | 8·40 | 11·90 |
| CaO | 0·02 | 0·05 | 0·00 | 0·17 (12) | 0·22 (02) | 0·10 (09) | 0·45 | 0·25 (15) | 0·01 | 0·01 |
| $Na_2O$ | 0·08 | 0·08 | 0·08 | 0·57 (05) | 0·99 (24) | 0·55 (06) | 0·70 | 0·63 | 0·44 | 0·50 |
| $K_2O$ | 10·28 | 10·14 | 10·15 | 8·68 (28) | 8·20 (31) | 8·37 (12) | 8·40 | 8·31 (25) | 9·20 | 9·10 |
| F | 2·19 | 2·34 | 1·67 | 0·74 | 1·00 (07) | 0·79 (09) | 0·42 | 0·32 (08) | — | — |
| Cl | 0·19 | 0·20 | 0·19 | 0·03 (0·02) | 0·05 (03) | 0·02 (03) | 0·04 | 0·00 | — | — |
| Total | 98·29 | 97·92 | 97·31 | 95·41 | 96·87 | 96·10 | 95·71 | 95·32 | — | — |
| O = F, Cl | 0·97 | 1·03 | 0·75 | 0·32 | 0·43 | 0·34 | 0·19 | 0·13 | — | — |
| Total | 97·32 | 96·89 | 96·57 | 95·09 | 96·44 | 95·77 | 95·53 | 95·19 | — | — |
| $H_2O$[*] | 2·9 | 2·9 | 3·1 | 3·6 | 3·5 | 3·6 | 3·7 | 3·7 | — | — |
| Total | 100·26 | 99·74 | 99·69 | 98·69 | 99·97 | 99·39 | 99·26 | 98·90 | — | — |
| $X_{Fe}$ | 0·47 | 0·47 | 0·51 | 0·44 | 0·55 | 0·47 | 0·56 | 0·62 | 0·63 | 0·47 |

[*] Water calculated to fill up the (OH, F, Cl) group.

Bishop Tuff data from Hildreth (1979). $X_{Fe}$ is Fe/ (Fe + Mg) cationic ratio. Numbers in parentheses following charge names are the number of replicate measurements averaged to obtain the reported analyses. Numbers in parentheses following oxide concentrations are 1 S.D. in terms of the last two units cited.

*Table 8 Representative compositions of natural and experimental clinopyroxene*

| | Lyngdal | | | | | | | | Bishop Tuff |
|---|---|---|---|---|---|---|---|---|---|
| | Natural | | Experimental | | | | | | |
| | | | 950°C | 850°C | 830°C | 950°C | 880°C | 830°C | |
| | 98N50 | 98N50 | 50-4 (2) | 50-9 | 50-25 (3) | 06-4 (2) | 06-18 (3) | 06-25 | |
| $SiO_2$ | 52·25 | 51·88 | 52·85 (14) | 49·80 | 50·89 (45) | 51·13 (1·46) | 51·06 (93) | 49·65 (83) | 52·00 |
| $TiO_2$ | 0·10 | 0·17 | 0·63 (08) | 0·69 | 1·17 (35) | 0·84 (32) | 0·42 (08) | 0·54 (33) | 0·15 |
| $Al_2O_3$ | 1·20 | 1·24 | 4·16 (78) | 4·31 | 4·74 (53) | 4·89 (59) | 2·60 (54) | 2·29 (31) | 0·75 |
| FeO | 12·24 | 12·29 | 10·01 (04) | 11·55 | 13·61 (70) | 9·89 (91) | 13 (50) | 14·97 (66) | 12·80 |
| MnO | 0·74 | 0·69 | 0·51 (04) | 0·73 | 0·60 (02) | 0·34 (03) | 0·34 (15) | 0·48 (09) | 0·55 |
| MgO | 11·32 | 11·23 | 12·42 (1·00) | 10·70 | 8·98 (54) | 11·79 (69) | 11·37 (36) | 9·78 (53) | 12·80 |
| CaO | 22·89 | 22·48 | 18·5 (01) | 20·06 | 18·42 (43) | 19·91 (74) | 19·27 (50) | 19·88 (46) | 20·60 |
| $Na_2O$ | 0·63 | 0·60 | 0·63 (06) | 0·54 | 0·65 (07) | 0·64 (10) | 0·44 (06) | 0·53 (10) | 0·38 |
| Total | 101·37 | 100·59 | 99·70 | 98·38 | 99·07 | 99·42 | 98·49 | 98·12 | 100·03 |
| En | 33 | 33 | 40 | 34 | 30 | 37 | 35 | 30 | 37 |
| Fs | 20 | 20 | 18 | 21 | 26 | 18 | 22 | 26 | 21 |
| Wo | 47 | 47 | 42 | 46 | 44 | 45 | 43 | 44 | 42 |

Bishop Tuff data from Hildreth (1979). Numbers in parentheses following charge names are the number of replicate measurements averaged to obtain the reported analyses. Numbers in parentheses following oxide concentrations are 1 S.D. in terms of the last two units cited.

*Table 9 Representative compositions of experimental low-Ca pyroxene*

| | Experimental | | | | | | | Bishop Tuff |
|---|---|---|---|---|---|---|---|---|
| | 950°C | 880°C | 830°C | 880°C | | 850°C | 830°C | |
| | 50-5(2) | 50-20 | 50-26 | 06-21 | 06-22(2) | 06-11 | 06-28 | |
| $SiO_2$ | 50·32 (1·02) | 48·68 | 49·26 | 49·83 | 51·38 (1·57) | 50·96 | 49·52 | 50·50 |
| $TiO_2$ | 0·98 (15) | 0·24 | 1·18 | 0·14 | 0·71 (59) | 0·15 | 0·76 | 0·13 |
| $Al_2O_3$ | 2·46 (14) | 1·56 | 1·27 | 1·02 | 2·71 (15) | 0·47 | 2·97 | 0·40 |
| FeO | 22·64 (1·51) | 27·53 | 32·27 | 28·65 | 28·29 (63) | 30·24 | 29·60 | 28·50 |
| MnO | 0·74 (05) | 0·87 | 0·73 | 0·75 | 0·53 (07) | 1·11 | 0·80 | 1·10 |
| MgO | 19·68 (77) | 15·60 | 12·94 | 12·43 | 10·28 (18) | 13·34 | 7·83 | 18·30 |
| CaO | 2·41 (05) | 2·44 | 2·21 | 5·44 | 5·53 (1·47) | 4·72 | 4·40 | 1·00 |
| $Na_2O$ | 0·11 (09) | 0·06 | 0·01 | 0·11 | 0·47 (00) | 0·22 | 0·63 | 0·02 |
| Total | 99·36 | 96·97 | 99·86 | 98·36 | 99·90 | 101·21 | 96·50 | 99·95 |
| Wo | 5 | 5 | 5 | 12 | 13 | 10 | 11 | 2 |
| Fs | 37 | 47 | 55 | 50 | 53 | 50 | 60 | 46 |
| En | 58 | 48 | 40 | 38 | 34 | 40 | 29 | 52 |

Bishop Tuff data from Hildreth (1979). Numbers in parentheses following charge names are the number of replicate measurements averaged to obtain the reported analyses. Numbers in parentheses following oxide concentrations are 1 S.D. in terms of the last two units cited.

*Table 10 Representative experimental glass analyses compared with the Bishop Tuff*

| | Experimental glasses | | | | | | | |
|---|---|---|---|---|---|---|---|---|
| | 1000°C | 950°C | 880°C | 850°C | 830°C | 775°C | 950°C | |
| | 50-43(6) | 50-3(6) | 50-20(5) | 50-9(5) | 50-26(5) | 50-30(4) | 06-3(7) | 06-20(5) |
| $SiO_2$ | 64·14 (63) | 68·01 (41) | 72·14 (45) | 71·75 (45) | 74·41 (46) | 72·96 (30) | 69·69 (34) | 71·43 (77) |
| $TiO_2$ | 1·12 (15) | 0·58 (07) | 0·23 (03) | 0·29 (03) | 0·14 (05) | 0·23 (12) | 0·55 (09) | 0·27 (14) |
| $Al_2O_3$ | 14·19 (25) | 15·65 (17) | 15·18 (22) | 15·22 (25) | 14·25 (13) | 14·90 (17) | 15·01 (16) | 15·25 (19) |
| FeO | 5·34 (39) | 3·28 (24) | 1·91 (38) | 2·13 (17) | 1·32 (31) | 1·34 (05) | 2·84 (17) | 2·16 (18) |
| MnO | 0·12 (08) | 0·11 (07) | 0·05 (05) | 0·11 (06) | 0·09 (07) | 0·10 (09) | 0·06 (05) | 0·02 (04) |
| MgO | 2·02 (10) | 1·00 (05) | 0·14 (02) | 0·27 (01) | 0·07 (02) | 0·10 (05) | 0·81 (03) | 0·22 (09) |
| CaO | 5·60 (44) | 3·39 (09) | 1·94 (07) | 2·51 (13) | 1·74 (16) | 2·08 (32) | 2·86 (17) | 2·05 (12) |
| $Na_2O$ | 3·66 (10) | 3·91 (19) | 3·78 (10) | 3·51 (38) | 3·37 (10) | 3·42 (12) | 3·37 (39) | 3·85 (07) |
| $K_2O$ | 3·78 (06) | 3·79 (18) | 4·57 (06) | 4·10 (08) | 4·43 (11) | 4·84 (16) | 4·55 (10) | 4·63 (15) |
| $P_2O_5$ | n.a. | 0·22 (07) | 0·04 (03) | 0·11 (09) | 0·16 (16) | n.a. | 0·19 (11) | 0·11 (05) |
| Total | 93·33 | 93·11 | 92·77 | 92·28 | 92·02 | 91·60 | 93·02 | 93·25 |
| $H_2O$ (melt) | 5·8 | 5·4 | 6·0 | 6·7 | 6·6 | 7·4 | 5·5 | 5·5 |

| | Experimental glasses | | | | | Whole-rock Bishop Tuff | |
|---|---|---|---|---|---|---|---|
| | 850°C | 830°C | 830°C | 775°C | FCT | | |
| | 50-10 (8) | 06-26 (8) | 06-28 (6) | 06-32 (5) | 49 (800°C) | Early | Late |
| $SiO_2$ | 72·71 (35) | 73·76 (48) | 75·37 (61) | 75·02 (54) | 73·11 | 77·40 | 75·50 |
| $TiO_2$ | 0·24 (03) | 0·16 (04) | 0·13 (05) | 0·07 (05) | 0·23 | 0·07 | 0·21 |
| $Al_2O_3$ | 14·64 (17) | 14·14 (20) | 13·02 (11) | 13·47 (1·57) | 14·59 | 12·30 | 13·00 |
| FeO | 1·90 (19) | 1·66 (22) | 1·60 (06) | 1·02 (08) | 1·49 | 0·70 | 1·10 |
| MnO | 0·03 (03) | 0·07 (06) | 0·06 (03) | 0·07 (09) | — | 0·04 | 0·02 |
| MgO | 0·26 (03) | 0·12 (03) | 0·09 (01) | 0·07 (04) | 0·21 | 0·01 | 0·25 |
| CaO | 2·05 (08) | 1·61 (13) | 0·99 (06) | 1·59 (61) | 1·67 | 0·45 | 0·95 |

| | | | | | | | |
|---|---|---|---|---|---|---|---|
| $Na_2O$ | 3·70 (13) | 3·50 (12) | 2·92 (09) | 3·30 (76) | 4·12 | 3·90 | 3·35 |
| $K_2O$ | 4·43 (08) | 4·91 (16) | 5·77 (07) | 5·38 (39) | 4·61 | 4·8 | 5·55 |
| $P_2O_5$ | 0·03 (10) | 0·06 (02) | 0·02 (02) | n.a. | n.a. | 0·01 | 0·06 |
| Total | 93·58 | 93·61 | 94·96 | 93·36 | 100 | 99·68 | 99·99 |
| $H_2O$ (melt) | 5·5 | 5·2 | 4·0 | 5·8 | — | — | — |

Compositions (wt %) of the experimental glasses normalized to 100. Bishop Tuff data from Hildreth (1979) and experimental glass from the FCT (Fish Canyon Tuff) from Johnson & Rutherford (1989*b*). Numbers in parentheses following charge names are the number of replicate measurements averaged to obtain the reported analyses. Numbers in parentheses following oxide concentrations are 1 S.D. in terms of the last two units cited. n.a., not analysed.

*Table 11 Modal proportions (wt %) of experimental and modelled mineral assemblages*

| Charge | *T* (°C) | *P* (kbar) | ΔNNO | Hbl | Cpx | Mt | Ilm | Pl | Bt | Ap |
|---|---|---|---|---|---|---|---|---|---|---|
| *Experimental mineral assemblages* | | | | | | | | | | |
| 06-5 | 950 | 4 | >2·5 | 0 | 30 | 16 | 12 | 40 | 0 | 2 |
| 50-20 | 880 | 4 | 0·03 | 39 | 14 | 15 | 3 | 25 | 0 | 5 |
| 50-9 | 850 | 4 | 0·59 | 45 | 14 | 19 | 5 | 10 | 0 | 6 |
| 50-25 | 830 | 4 | –0·01 | 59 | 0 | 9 | 4 | 23 | 1 | 4 |
| 50-26 | 830 | 4 | –0·11 | 49 | 2 | 9 | 4 | 32 | 1 | 4 |
| 06-25 | 830 | 4 | 0·01 | 36 | 4 | 11 | 3 | 0 | 40 | 5 |
| 50-34 | 850 | 2 | >1·5 | 7 | 14 | 20 | 5 | 48 | 4 | 3 |
| 50-48 | 850 | 2 | 1·5 | 21 | 12 | 21 | 4 | 34 | 5 | 4 |
| *Modelled mineral assemblages* | | | | | | | | | | |
| Step 1 (model 1) | | | | 22 | 13 | 12 | 3 | 47 | 0 | 4 |
| Step 1 (model 2) | | | | 0 | 23 | 14 | 4 | 56 | 0 | 3 |
| Step 2 | | | | 11 | 5 | 10 | 1 | 60 | 10 | 3 |

Modelled mineral assemblages from Bogaerts *et al*. (2003*a*). Pl, plagioclase; Hbl, hornblende; Cpx, clinopyroxene; Bt, biotite, Mt, magnetite; Ilm, ilmenite; Ap, apatite.